

**Title: Structures from intact myofibrils reveal mechanism of thin filament
regulation through nebulin**

Authors: Zhexin Wang^{1,†}, Michael Grange^{1,†,‡}, Sabrina Pospich¹, Thorsten Wagner¹, Ay Lin Kho², Mathias Gautel², Stefan Raunser^{1,*}

Affiliations:

¹Department of Structural Biochemistry, Max Planck Institute of Molecular Physiology, Otto-Hahn-Strasse 11, 44227, Dortmund, Germany

²Randall Centre for Cell and Molecular Biophysics, School of Basic and Medical Biosciences, Kings College London BHF Centre of Research Excellence, New Hunt's House, Guy's Campus, London SE1 1UL, UK

[‡]Current address: Structural Biology, The Rosalind Franklin Institute, Harwell Science and Innovation Campus, Didcot OX11 0FA, UK

[†]The authors contributed equally

*To whom correspondence should be addressed: stefan.raunser@mpi-dortmund.mpg.de

Abstract

In skeletal muscle, nebulin stabilises and regulates the length of thin filaments, but the underlying mechanism remains nebulous. Here, we used electron cryo-tomography and subtomogram averaging to reveal structures of native nebulin bound to thin filaments within intact sarcomeres. This in situ reconstruction provided high-resolution details of the interaction between nebulin and actin, demonstrating the stabilising role of nebulin. Myosin bound to the thin filaments exhibited different conformations of the neck domain, highlighting its inherent structural variability in muscle. Unexpectedly, nebulin did not interact with myosin or tropomyosin, but with a troponin-T linker through two potential binding motifs on nebulin, explaining its regulatory role. Our structures support the role of nebulin as a thin filament “molecular ruler” and provide a molecular basis for studying nemaline myopathies.

One-Sentence Summary:

In situ cryoET structures of muscle thin filaments elucidate the structural and regulatory role of nebulin.

Main text

Nebulin is a major structural protein of skeletal sarcomeres and is essential for proper assembly and contraction of skeletal muscle (1). A sarcomere is composed of thin filaments comprising mainly F-actin, tropomyosin, and troponin and myosin-containing thick filaments. Thin and thick filaments are organised into morphologically distinct zones. The Z-disc and M-band mark the boundary and centre of a sarcomere, respectively. Proximal to the Z-disc is the I-band which contains only thin filaments. Between the M-band and the I-band, myosin cross-bridges are formed between thin and thick filaments in the A-band (Fig. S1A) (2). A single nebulin molecule (molecular weight over 700 kDa) has been proposed to bind along the entire thin filament from the Z-disc to near the M-band (3, 4), maintaining the stability of thin filaments (5). Mutations in its encoding gene, NEB, are a major cause of a class of skeletal muscle disorders termed nemaline myopathies that present with a range of pathological symptoms such as hypotonia, muscle weakness and, in some cases, respiratory failure leading to death (6–8). Despite the critical role of nebulin in skeletal muscle, nebulin is only minimally expressed in cardiac muscle (9), where instead nebulin, a short homolog of nebulin, is present but only close to the Z-disc. The absence of nebulin results in a broader range of thin filament length (10) in cardiomyocytes that possibly enables greater tunability of activation (11).

Nebulin primarily consists of 22-28 tandem super repeats. Each super repeat consists of 7 simple repeats, each made of 31-38 amino acid residues, featuring a conserved sequence motif SDxxYK (12, 13). The N- and C-termini of nebulin associate with the capping proteins on the two ends of the thin filaments, tropomodulin (towards the M-band) (14) and CapZ (at the Z-disc) (15), respectively. Nebulin is thus hypothesised to regulate thin filament length as a “molecular ruler”, albeit with the exact mechanism remaining unknown (5, 16–19). Indeed, genetic ablation of nebulin in mice is lethal and results in sarcomeres with loss of their length-regulation (20, 21).

It has been suggested that, based on the modular sequence of nebulin, each simple repeat would bind to one actin subunit and every seventh repeat, i.e. a super repeat, would interact with the tropomyosin-troponin regulatory complex (12). However, structural details of these interactions and native nebulin are lacking. It thus remains unclear how nebulin stabilises or regulates thin filaments. The enormous size of nebulin combined with its elongated and flexible nature has prevented the use of in vitro reconstituted systems of nebulin and thin filaments that would resemble the native state in a sarcomere. Recombinant nebulin fragments bind to and bundle F-actin, (22), precluding a reconstitution approach for electron-microscopical structural biology.

Here, we imaged nebulin directly inside mature mouse skeletal sarcomeres from isolated myofibrils using cryo-focused-ion-beam milling (cryo-FIB) and electron cryo-tomography (cryo-ET).

In situ position of nebulin on thin filaments

We determined the structure of the core of the thin filament from intact myofibrils isolated from mouse psoas muscle to 4.5 Å resolution and with actomyosin resolved to 6.6 Å resolution (Fig. S1,2). In the core of the thin filament, two extra continuous densities were visible alongside the actin filament (Fig. 1A-C). The elongated structure predicted for nebulin (23) suggested that this density might be natively organised nebulin bound to the thin filament. To verify this putative identification, we determined the in situ actomyosin structure in the A-band from cardiac muscle (Fig. S3A,B). Nebulin is barely expressed and only present in small subpopulations of myofibrils in cardiac muscle. The averaged reconstruction of the cardiac thin filament, determined to an overall resolution of 7.7 Å with the core of the thin filament resolved to 6.3 Å, depicts similar organisations of actin, myosin and tropomyosin. Notably, the extra density observed in skeletal

actomyosin was missing (Fig. 1E), consistent with this density corresponding to averaged segments of nebulin.

Nebulin was observed in the grooves between the two strands of the actin filament, following their helical turn (Fig. 1A). Nebulin occupies a site that is known to be bound by actin-stabilising compounds such as phalloidin and jasplakinolide (24) (Fig. S4). This may explain why excessive phalloidin can unzip nebulin from thin filaments (25) and may also suggest a similar mechanism of F-actin stabilisation. Similar to phalloidin, nebulin binding to F-actin did not alter the helical arrangement of F-actin or the conformation of the actin subunits (Fig. 2A,B). A single actin filament was decorated by two nebulin molecules on the opposite sides (Fig. 1B). In order to ascertain the molecular organisation of nebulin in different regions of a sarcomere, we also determined the structure of the thin filament in the skeletal muscle I-band to a resolution of 7.4 Å (Fig. S3C,D). Nebulin appeared in the I-band at the same position on the thin filament as was observed within the A-band (Fig. 1D), indicating that nebulin spans most of the thin filament (18, 26). This suggests that nebulin maintains a structural role within the sarcomere. Notably, the position of nebulin bound to actin from native skeletal muscle is different from the three putative sites previously proposed on the outer surface of the actin filament based on reconstituted actin-nebulin fragment complexes (27). The observed differences could represent the limitations of the use of in vitro fragments of nebulin or suggest different interaction patterns during sarcomerogenesis.

The position of nebulin implies that it does not interact with tropomyosin (Fig. 1B). The subdomain 3 and 4 (SD3, 4) of adjacent actin monomers physically separate nebulin from tropomyosin, regardless of the tropomyosin state at different Ca^{2+} concentrations (28) (Fig. 2C-F). This is contradictory to previous results from in vitro experiments (29). The discrepancy between our in situ structures and in vitro assays again demonstrates that nebulin may have different

properties when purified, compared to its native state in a sarcomere. Purified large fragments of nebulin are extremely insoluble when expressed (22, 30, 31). Both rotary shadowed images of nebulin (31) and the structure of nebulin predicted by the machine-learning-based software, AlphaFold (32), suggest non-filamentous structures. These visualisations clearly deviate from the elongated shape of nebulin when bound to actin filaments. Our approach of investigating nebulin inside sarcomeres thus provides in situ structural information about nebulin interactions with the thin filament that are not accessible by sequence-based structure prediction programs or from isolated proteins. Furthermore, during sarcomerogenesis, nebulin integration into the thin filament is likely to require cellular cofactors to prevent the formation of aggregates or large globular structures.

Myosin double-head does not interact with nebulin and has high variability

Nebulin has been shown to regulate the actin-myosin cross-bridge cycle. It can increase thin filament activation, promote myosin binding and thus improve the efficiency of contraction (33–35). In vitro studies have suggested a direct interaction between a nebulin fragment and myosin (36, 37). In our rigor state sarcomere structures, two myosin heads from a single myosin molecule are bound to the thin filament in most cross-bridges, forming a double-head. However, the myosin heads do not interact with nebulin (Fig. 1A) nor does nebulin alter the interactions between actin and myosin (Fig. S5B).

Having a better-resolved structure available (~ 9 Å in the neck domain), we were able to accurately fit the lever arms and light chains of myosin based on their secondary structure elements (Fig. S5D-F), completing the model of the entire myosin double-head (Fig. 3A, S5). Notably, the angles of the kinks in the lever arm helix are different between the two heads (Fig. 3A). Especially the kink between the two regulatory light chain (RLC) lobes differs considerably in the two heads,

resulting in the clamp-like arrangement of the neck domains (Fig. 3B). The RLC-RLC interface resembles that of the RLCs of the free and blocked head in an interacting-head-motif (IHM) of an inactive myosin (38, 39), but with a rotation of $\sim 20^\circ$ (Fig. 3C). Although the motor domains are similarly arranged in the cardiac muscle (Fig. S6A), our 12 Å reconstruction of the neck domain clearly demonstrates that the interface between the two RLCs is different compared to the skeletal counterpart, resulting in a subtle difference in the arrangement of the two neck domains (Fig. S6B). Thus, our structures of myosin in the ON state in skeletal and cardiac muscles and previous structures of myosin in the OFF state (38, 39) imply natural variabilities within RLCs and at the RLC-RLC interface that allow a dynamic cooperation between the two myosin heads.

We noticed that 18% of the skeletal double-heads had a different conformation in which both neck domains are bent by $\sim 20^\circ$ perpendicular to the direction of the myosin power stroke (Fig. 3D,E, S7A). This different structural arrangement increases the range within which myosin can bind to the thin filament by ~ 5 nm without interfering with force transmission during the power stroke (Fig. 3F). Thus, the bending contributes additional adaptability on top of what is provided by the flexibility of the S2 domain for cross-bridge formation between actin and myosin filaments (Fig. 3G). The myosin “arm” can thus hold on tightly to a thin filament, but at the same time have enough freedom to cooperate the mismatch between helical pitches of thick and thin filaments and account for local deformation of the sarcomere. Indeed, the double-heads with bent neck domains are randomly distributed in the A-band of the sarcomere (Fig. S7B-D), ensuring efficient binding of myosin during contraction.

Nebulin structure and localisation of residues

While nebulin consists of repetitive simple repeats, each simple repeat has different sequences, with a few conserved charged residues and a putative actin-binding SDxxYK motif (Fig. 4A,G,

S8A). Owing to the nature of sub-tomogram averaging, the obtained EM density map of nebulin is an averaged density of all repeats in the A-band. Taking advantage of the 4.5 Å map, where bulky side chains are typically resolved (Fig. S2), we were able to build an atomic model for actin and refine a poly-alanine nebulin model into its density (Table S1). Using a published convention (12), we defined the start of a simple repeat at two residues preceding a conserved aspartic acid, resulting in the SDxxYK motif residing at position 18-23.

The model of nebulin consists of a repetitive structure of two α -helices (H1 and H2), with a short kink of 46° in between, followed by a loop region spanning around SD1 of actin (Fig. 4B-D). As validation, and in order to map the sequence to our structural model, we predicted the average secondary structure to highlight structured and unstructured regions from the sequences of nebulin simple repeats (Fig. S8B, Methods). The prediction implied each nebulin simple repeat should form a long helix, with a drop in probability in the middle of this helix (Fig. 4F). By matching the predicted start of the helix in the sequence with the start of H1 in the structure, the predicted end of the helix matched the end of H2 and the dip in probability matched the position of the kink in our model (Fig. 4E, F). Based on this registry, a noticeable bulky side chain density aligned with position 22, corresponding to a fully conserved tyrosine residue. We attributed this density as the phenyl group of this tyrosine (Fig. 4E, Fig. S2D). This observation further validates the sequence-structure mapping. As such, H1 starts at position 5, which is often occupied by a proline (Fig. 4E-G). The SDxxYK motif, where the exon boundaries are, is located at the beginning of H2, among which the serine is positioned at the kink between H1 and H2. This registry allowed us to assign the location of other conserved residues, and further investigate their roles in the interactions between nebulin and the thin filament.

Nebulin as a “molecular ruler” of the thin filament

A molecular ruler for the actin filament should coordinate two main functions: capping of the barbed and pointed end of the filament at a defined distance and being in close association with actin subunits along the filament length. Although the general concept of nebulin being a “molecular ruler” is supported by its size being proportional to the length of the thin filament in different muscle fibres (16, 40), it has been speculated that the interaction of nebulin with the thin filament differ at the N- and C-termini (14, 15). Because we averaged over all nebulin repeats, our study does not give insights into the ends of nebulin. However, the structures of the native thin filaments clearly depict a 1:1 stoichiometry between nebulin repeats and actin subunits in both A-band and I-band (Fig. 1D,4D). Furthermore, the repeats are distinct structural units rather than part of a contiguous α -helix, as previously suggested (23). Thus, each nebulin repeat likely denotes the “gradation” of a ruler in measuring the number of actin subunits.

While most nebulin simple repeats contain 35 amino acids (as is modelled above), some repeats can be as short as 31 aa or as long as 38 aa (Fig. S8C). Different sizes of nebulin repeats typically correspond to different positions in a super repeat (Fig. 4B). The predicted secondary structure implies that in the shorter repeats, the helix ends earlier than in an average-length repeat and in the longer repeats, the loop is longer (Fig. S8D). Although we did not observe separate classes within our cryo-ET data for these repeats owing to their low abundance, it is noticeable that the density corresponding to H2 and the first half of the loop has lower occupancy compared to H1 (Fig. S8E). This suggests that in the shorter nebulin repeats, part of H2 is extruded into the loop along segments of actin to compensate for fewer amino acids while in the longer nebulin repeats, the extra amino acids reside flexibly in the loop (Fig. S8F). This ensures that in all regions of the sarcomere, nebulin repeats have the same physical length to span an actin subunit to maintain a 1:1 binding stoichiometry which is one of the main functions of a “molecular ruler”.

Interactions between nebulin and the thin filament

Based on our model, we were able to show that the interactions between actin and nebulin are mediated by residues throughout one nebulin simple repeat and three adjacent actin subunits (Fig. 5A). In the SDxxYK motif, Y22 forms a potential cation- π interaction with K68 on SD1 of one actin subunit (N) (Fig. 5C). S18 likely forms a hydrogen bond with E276 on SD3 of the laterally adjacent actin subunit on the other strand (N+1). D19 and K23 interact with residues on SD1 and SD2 of actin subunit N through electrostatic attractions. In addition, other highly conserved charged residues outside the SDxxYK motif are also involved in the interactions between actin and nebulin. D3, K11 and K30 can form electrostatic interactions with SD1 of actin subunit N+2, SD4 of actin subunit N+1 and SD1 of actin subunit N, respectively (Fig. 5C). Every nebulin repeat interacts with all three neighbouring actin subunits (Fig. 5A), which prevents them from depolymerisation and confers rigidity and mechanical stability to the thin filament.

We noted that an intra-molecule interaction occurs between position 15 and 21 on nebulin at the position of the kink between H1 and H2 (Fig. 5A,B). Although both positions can accommodate either positively or negatively charged residues, they appear to be often complementary to each other among all repeat sequences (Fig. S9A-C). Their interaction is also supported by weak side-chain densities in our averaged reconstruction (Fig. S9D). This intra-molecular interaction stabilises the kink conformation of the two helices, which is necessary for positioning charged residues near actin.

Nebulin simple repeats share a higher sequence similarity with the repeats that are six repeats apart, forming a seven-repeat super repeat pattern (Fig. 4A). This modular structure suggests an interaction with the troponin-tropomyosin regulatory complex, which also has a 1:7 stoichiometry ratio to actin. The physical separation by actin between nebulin and tropomyosin has ruled out their interactions. The core of troponin, including troponin C (TnC), troponin I (TnI)

and the majority of troponin T (TnT) are also located away from nebulin (Fig. 6A). On the other hand, a linker region in TnT between R134 and R179 is likely to be the binding partner of nebulin (Fig. 6C). It was hypothesised to cross the groove between two actin stands (41). Although nebulin and this TnT linker could not be resolved in a structure of the thin filament containing troponin determined from our data (Fig. S10), previous structures of troponin with actin, reported from cardiac thin filament (42, 43), show that this TnT linker is localised close to the region where nebulin resides in our structure. Despite the lack of a structural model for the linker owing to its flexibility, superimposing previous EM densities for TnT with our structural model of actin and nebulin suggests the location of two contact sites between TnT and nebulin (Fig. 6A,B). One site is located at the end of H2 (Fig. 6A-C box I). This site is consistent with the position of a WLKGIGW motif in nebulin, which has previously been proposed to be the tropomyosin-troponin binding motif at the end of repeat 3 (12). The other site is located downstream of the first site at the start of H1, indicating another potential troponin-binding motif, ExxK, at the beginning of repeat 4 (Fig. 6A-C box II). The TnT linker region contains a hydrophobic C-terminus and a highly charged N-terminus matching the orientation of the two binding sites, suggesting the WLKGIGW motif and ExxK motif interact with TnT through hydrophobic and electrostatic interactions, respectively (Fig. 6D).

Although missense mutations have not been localised to this linker, TnT is the only Tn component where mutations can lead to nemaline myopathy (7). For example, Amish nemaline myopathy, a severe type, is caused by a TNNT1 (slow muscle troponin) truncation (44) and a splicing variant of TNNT3 (fast muscle troponin) can also lead to nemaline myopathy (45). This is in agreement with our proposed interactions between nebulin and TnT. Based on our observation that nebulin does not interact with myosin or tropomyosin, the role nebulin plays in regulating myosin binding is likely to be a downstream effect of its interaction with the TnT linker. This

interaction in skeletal muscle may rigidify the linker and thus help to maintain efficient calcium regulation and the subsequent binding of myosin. It can also increase the cooperativity in calcium regulation across the two actin strands, which has been recently observed in cardiac muscle (43).

Human nebulin and insights into nemaline myopathy

Nebulin in mouse shares more than 90% sequence similarity with human nebulin (46). Key residues involved in the interactions between nebulin and the thin filament are conserved among repeats of mouse and human nebulin (Fig. S11). Our structural model of nebulin derived from mouse is thus also applicable to human and enables the understanding of the mechanism underlying the pathogenicity caused by recessive mutations in the NEB gene, which is the major cause of nemaline myopathies (7). Nemaline myopathy mutations are usually compound heterozygous, in some cases with one truncating and one missense variant (7). Two missense NEB mutations, Ser6366Ile and Thr7382Pro, have been identified as founder mutations in the Finnish population (47). The locations of the two sites on a simple repeat correspond to Ser18 and Thr14 (Fig. S9E). A mutation of Ser18 into a hydrophobic isoleucine would disrupt its potential hydrogen bond with actin (Fig. 5C, S9F). A mutation of Thr14 to proline, despite not being at a conserved residue position, can lead to the disruption of H1 helical secondary structure and thus alter the local conformation of nebulin and interfere with actin binding (Fig. S9F).

Our structural model of actin and nebulin maps residues crucial in maintaining the interactions between nebulin and the thin filament. When also applied to clinical genetics, this information should help to determine additional pathogenic interfaces of nebulin variants. This is especially crucial when considering missense variants, where the pathogenicity is often difficult to determine (47) and will thus aid the early diagnosis of nemaline myopathies and genetic counselling of variant carriers.

Conclusions

Our structural reconstruction of nebulin within a native skeletal sarcomere provides the basis of interaction between nebulin and thin filaments. Our structures determined across several tissue types and regions enable a comparative analysis of nebulin in its native context. It reveals the mechanism underlying the roles nebulin plays in regulating thin filament length, as a thin filament stabiliser, as well as in regulating myosin-binding through its interaction with TnT. Our approach using cryo-FIB milling and cryo-ET, provides a high-resolution structural approach within an isolated tissue. Our findings highlight different conformations of myosin and illustrates similarities and differences from in vitro structures. Together with the recent study reporting the high-resolution structure of bacterial ribosomes (48), our structures showcase the full potential of in situ structural biology using cryo-ET. In the context of the sarcomere where several flexible proteins, such as titin and myosin-binding protein-C, are present and still lack structural visualisation, our approach is a general tool for structural analysis where other methods are limited. Determining the structure of these key players in the context of native sarcomeres will enable better modelling of skeletal muscle in the future, directly impacting also the understanding of disease. The structure of nebulin presented here is one such case, where the molecular interactions described might help to establish a foundation for future developments of the treatment of nemaline myopathies.

Materials and Methods

Myofibril isolation

Skeletal myofibrils were prepared from pre-stretched BALB/c mouse psoas muscle fibre bundles
5 as described previously (2).

Cardiac myofibrils were prepared from left ventricular trabecular strips pre-stretched overnight to
a sarcomere length of about 2 μm in rigor buffer (20 mM HEPES pH 7, 140 mM KCl, 2 mM
MgCl₂, 2 mM EGTA, 1 mM DTT, Roche complete protease inhibitor) at 4°C. Left ventricles were
cut into ~1 mm pieces using scalpel blades and homogenised first in rigor buffer with complete
10 protease inhibitors, then resuspended and homogenised 3-4 times in rigor buffer containing 1%
(v/v) Triton X-100 essentially as described (49). Dissociation into myofibril bundles containing 3-
5 myofibrils was monitored by microscopy. The concentration of myofibrils was adjusted with
complete rigor buffer to ~5 mg/mL, using an extinction coefficient of myofibrils in 1% (w/v) warm
SDS solution of ~0.7 mL mg⁻¹cm⁻¹. Both cardiac myofibrils and skeletal myofibrils were prepared
15 from 3-month female BALB/c mice, and myofibrils from both tissues were prepared from the same
animal for each biological replicate.

Vitrification of myofibrils and cryo-focused ion beam milling

Myofibrils were frozen on grids by plunge-freezing using a Vitrobot. Generally, 2 μl of myofibril
20 suspension was applied onto the glow-discharged carbon side of Quantifoil R 1.2/1.3 Cu 200 grids.
After a 60-second incubation at 13°C, the grids were blotted from the opposite side of the carbon
layer for 15 seconds before plunging into liquid ethane. For the dataset aimed at determining the
I-band thin filament structure, myofibrils were frozen on Quantifoil R 1/4 Au 200 grids with SiO₂

film after a longer blotting time of 20 seconds. Frozen grids were clipped into cryo-FIB-specific AutoGrids with marks for grid orientation and a cut-out for low angle FIB-milling.

Clipped grids were transferred into an Aquilos cryo-FIB/SEM dual-beam microscope (Thermo Fisher). Cryo-FIB-milling was performed as previously described (2). Briefly, the grids were first sputter-coated with platinum and then coated with metalloorganic platinum through a gas-injection-system. The myofibrils were thinned into lamellae in a four-step milling process with an ion beam of decreasing current from 0.5 μ A to 50 nA. For the dataset of I-band thin filaments, AutoTEM was used to automatically produce lamellae with thicknesses of 50-200 nm. During auto-milling, an anti-contamination shield replacing the original shutter was inserted to minimise contamination from water deposition (50).

Electron cryo-tomography data acquisition

Grids containing milled lamellae were transferred through a low-humidity glovebox (50), in order to avoid contamination, into a Titan Krios (Thermo Fisher) transmission electron microscope equipped with a K2 Summit or K3 camera (Gatan) and an energy filter. Projection images were acquired using SerialEM software (51). Overview images of myofibrils in lamellae were acquired at 6,300 x or 8,400 x nominal magnification to identify locations for high-magnification tilt series acquisition and serve as reference images for batch tomography data acquisition. Tilt series of the skeletal A-band dataset were acquired at 81,000 x nominal magnification (pixel size 1.73 Å, calibrated based on an averaged reconstruction and a crystal structure of myosin (PDB: 3I5G) (52)) with the K2 Summit camera. Tilt series of the cardiac A-band dataset and the skeletal I-band dataset were acquired with the K3 camera, at 42,000 x (pixel size 2.23Å) or 81000 x (pixel size 1.18 Å) nominal magnification, respectively. A dose-symmetric tilting scheme (53) was used

during acquisition with a tilt range of -54° to 54° relative to the lamella plane at 3° increments. A total dose of $130\text{-}150\text{ e}^{-}/\text{\AA}^2$ was applied to the sample.

Tomogram reconstruction and automatic filament picking

Individual tilt movies acquired from the microscope were motion-corrected (54) and combined into stacks for a given tomogram with matched angles using a custom script for subsequent tomogram reconstruction. The combined stacks were then aligned, CTF corrected through strip-based phase flipping and reconstructed using IMOD (55). In total, three datasets were collected: skeletal (psoas) A-band (171 tomograms), cardiac A-band (24 tomograms) and skeletal I-band (115 tomograms). Tomograms containing wrong field of view, incompletely vitrified ice or lacking visible inherent sarcomere features due to the lamella being too thick ($>150\text{ nm}$) were discarded. Eventually, 48, 24 and 47 tomograms were selected from skeletal A-band, cardiac A-band and skeletal I-band datasets, respectively, for further processing.

Automated picking of mouse psoas A-band: The picking of thin filaments within the mouse psoas A-band was performed as previously outlined(2). Briefly, tomograms were re-oriented so that the thin and thick filaments of the sarcomere lay along the Y axis of the volume and such that XY slices contained the central section of the thin and thick filaments. After applying an equatorial filter as a Fourier mask, thin filaments were recognised and traced from the XZ slices by the TrackMate plugin (56) in Fiji (57, 58). In total, 183,260 segments of the thin filaments (subtomograms) were picked from 48 tomograms with an inter-segment distance of 62 \AA . The distance was determined to accommodate two adjacent actin subunits on one strand for further averaging of myosin double-head structure.

Automated picking of mouse cardiac A-band: The picking of the mouse cardiac A-band thin filament used a similar approach as described above for skeletal A-band, with the following changes: after the rotation of the tomograms, from the XZ slices, positions of the thin filaments were determined using crYOLO (59) instead of TrackMate. Manual picking of thin filaments from 28 XZ slices from 6 tomograms were used for initial training in crYOLO. The positions for thin filament in all tomograms were then picked and traced by crYOLO. In total, 202,864 segments of the thin filaments were picked from 24 tomograms with an inter-segment distance of 65 Å.

Automated picking of mouse psoas I-band: The picking of the mouse psoas I-band was performed using the latest development version of crYOLO (1.8.0b33) to pick directly on XY slices without any pre-rotation of tomograms. Tomograms were reconstructed using the program Warp after alignment in IMOD, at a down-sampled scale of 8x. Thin filaments were manually picked on 21 XY slices from 4 tomograms. These picked positions were then used to train a model in crYOLO which was used to pick all tomograms. The picked positions were then traced through different XY planes in 3D. In total, 84,937 segments of I-band thin filaments were picked from 47 tomograms with an inter-segment distance of 38 Å.

Sub-tomogram averaging

Skeletal A-band thin filament: Sub-tomogram averaging of the skeletal A-band thin filaments first followed a previously published approach (2). Briefly, the determined positions for filaments within the tomograms were used to extract sub-tomograms in RELION (60) using a box size of 200 voxels (346 Å), which were then projected (central 100 slices) and sorted into good and bad particle classes through 2D classification in ISAC (61). Good particles were then subject to three-

dimensional refinement using a cylindrical reference in RELION, achieving a global resolution (0.143 criterion) of 8.8 Å.

In order to increase resolution, the particles were then subjected to further refinement in the program M (62). Tilt movies and image stacks were motion-corrected and CTF-estimated within Warp (63) and new tomograms were reconstructed. The original particle position information obtained from the final step of refinement in RELION was then transformed to match the output geometry of tomograms from Warp. The new particles were extracted in Warp for subsequent averaging in RELION using a 2x down-sampling. After 3D refinement in RELION, the structure of the thin filament was determined to 7.8 Å (Fig. S1). The final half-maps and alignment parameters were subjected to M for refinement. The strategy for refinement in M followed previously published regimens (62). After this refinement, the structure reached a global resolution of 6.7 Å. The core of the thin filament, including actin and nebulin, was masked and reached a resolution of 4.5 Å (Fig. S1,S2), which was used for model building of actin and nebulin.

Skeletal A-band actomyosin and myosin neck domain. In order to resolve the actomyosin structure, including thin filament and a bound myosin double-head, a 3D classification approach similar to the one previously published (2) was used. After the refinement in M, sub-tomograms were re-extracted and classified in RELION. Classes were translated and rotated to a common double-head configuration and re-refined in M. The final reconstruction at a resolution of 6.6 Å was used for model building of myosin heavy chain. In order to increase the resolution of the myosin neck domains (predominantly the ELC and RLC), the sub-tomograms were first re-centred towards ELC and re-refined in RELION with a mask containing only myosin. This resulted in an ELC-centred myosin double-head structure with a resolution of 8.9 Å (Fig. S1). Afterwards, the sub-tomograms

were further re-centred towards RLC and re-refined with a smaller mask containing ELCs and RLCs to reconstruct a structure of RLC-centred myosin double-head with a resolution of 9 Å. The ELC- and RLC-centred myosin double-head maps were used for rigid-body docking of ELC and RLC models, respectively.

5

Cardiac A-band thin filament, actomyosin and myosin neck domain: Sub-tomogram averaging of the cardiac A-band thin filament followed the same strategy as for the A-band of skeletal muscle and resulted in a structure of thin filament resolved to a global resolution of 8 Å, with the core of thin filament (actin) resolved to 6.3 Å (Fig. S3A,B). Structures of cardiac actomyosin and myosin neck domain were determined using the same classification and re-centring approach as for skeletal structures, resulting in resolutions of 7.7 Å and 12 Å, respectively.

10

Skeletal I-band thin filament: Sub-tomogram averaging of the skeletal I-band thin filament excluding troponin was performed largely as described for the A-band structures, except for using helical symmetry (twist -167.4°, rise 28.8 Å) during the initial refinement in RELION to reduce alignment error due to the missing wedge artefacts. The final structure of the I-band thin filament was determined to a global resolution of 9.4 Å, with the core (actin and nebulin) resolved to 7.4 Å (Fig. S3C,D). Sub-tomogram averaging of the thin filament including troponin was performed as previously described (2). 2,030 manually-picked sub-tomograms were used for averaging using a cylinder-like reference generated from averaging all particles without alignment.

15

20

Model building of actin, nebulin and myosin heavy chain

To reduce the risk of over-refinement and account for the heterogenous resolution of our structures, several density maps, which were masked to different areas, filtered to nominal or local resolution

as determined by SPHIRE (64) and sharpened using various B-factors, were used for model building. In addition, density modified maps were calculated from half maps providing the reported nominal resolution (65).

5 An initial model for actin was generated by homology modelling using Modeller (66) in Chimera based on a previous atomic model (PDB: 5JLH (67), chain A) and a sequence alignment from Clustal Ω . The unresolved N-terminus of actin (aa 1-6) was removed and Mg^{2+} -ADP was added from PDB 5LJH. HIS 73 was replaced by HIC (4-methyl-histidine) and regularized in Coot (68). A pentameric composite model was assembled by rigid-body fitting in Chimera including an initial
10 model of nebulin (see below). Model building was performed in ISOLDE (69) in ChimeraX (70). A total of four density maps were loaded (filtered to nominal resolution and sharpened with B-factors -70 and -150; filtered to local resolution and sharpened to B-factor -100; and the density modified map). Only the central actin chain and residues in close contact were included in the simulation and rebuilt. Unresolved side chains are in the most likely positions. After a first pass
15 through the complete molecule, Ramachandran and rotamer issues were addressed locally. Based on the refined central chain, the composite actin-nebulin pentamer was updated. Hydrogens were removed and the resulting model was real-space refined against the map filtered to nominal resolution in Phenix (71). To avoid large deviations from the input model, the ISOLDE model was used as a reference, while local grid search, rotamer and Ramachandran restraints were
20 deactivated. The actin model was further improved by a second round of model building in ISOLDE.

Modeling of nebulin was performed in analogy. An initial poly-alanine model for nebulin was built manually in Coot based on the density of the central repeat (4.5 Å resolution). In order to

cover the connection between two nebulin repeats, a peptide of 56 aa (instead of 35 aa) was initially built. The density corresponding to residue 22 was consistent with a consensus tyrosine residue and thus tyrosine was used instead of alanine. A segmented post-processed map (filtered to nominal resolution and sharpened with B-factor -70) was loaded for further modelling in ISOLDE.

5 Secondary structure and rotamer restraints were applied where appropriate. Based on the resulting model, a continuous model of nebulin was created by first cutting the model to 35 aa and rigid-body fitting into the density. The termini of three consecutive nebulin chains were then manually connected. To address geometry issues due to the connection, the combined nebulin chain was real-space refined in Phenix against the segmented map and subjected to another round of
10 refinement in ISOLDE.

Refined models of actin and nebulin were finally combined into one pentameric model. Minor adjustments to the orientation of side chains were done in Coot where necessary. The composite model was real-space refined against the 4.5 Å-resolution map filtered to local resolution (B-factor
15 -100) in Phenix using the same settings as before.

An initial model of the actin-nebulin-tropomyosin-myosin (actomyosin) complex was assembled from the refined actin-nebulin model, a homology model of myosin (52) (PDB: 3I5G, chain A), and a polyalanine model of tropomyosin (67) (PDB: 5JLH chains J and K) using rigid-body fitting.

20 Only the heavy chain of myosin (up to residue 788) was modelled. After addition of hydrogens, the central myosin chain was refined in ISOLDE using four segmented density maps of actomyosin, as described for actin. All applicable secondary structure restraints and many rotamer restraints were applied. Manual building was started from the acto-myosin interface, as it is best resolved. Unresolved residues including loop I (aa 207-215), loop 2 (626-643) and the N-terminus

(1-11) were removed. After deletion of hydrogens, the resulting atomic model was real-space refined in Phenix and further improved by a second round of refinement in ISOLDE. The refined atomic model of the central myosin chain, was finally used to assemble an updated composite model of the actomyosin complex. This model was addressed to a final round of real-space refinement in Phenix against a 6.6 Å-resolution density map filtered to nominal resolution (B-factor -75) using the same settings as before, but with both Ramachandran and Rotamer restraints applied.

As the resolution was not sufficient to reliably model Mg^{2+} ions, they were replaced with the ones from PDB 5JLH by superposition of actin subunits. The final atomic models of actin-nebulin and actomyosin complexes were assessed by Molprobit (72) and EMRinger (73) statistics ([Table S1](#)).

Rigid-body docking of myosin light chains

As the density for the C-terminus of the myosin heavy chain lever arm as well as the ELC and RLC is of insufficient quality for reliable model building with refinement, rigid-body docking of previously published structural models (52) (PDB: 3I5G) was performed. First, the ELC model together with the ELC-binding lever arm helix (aa 785-802 in PDB 3I5G) were docked into both myosin ELC densities in the ELC-centred myosin double-head map (8.9 Å, B-factor -500) in Chimera. Then, the RLC model together with RLC-binding HC helices (aa 809-839) were docked into the RLC density of the leading myosin head in the RLC-centred myosin double head map (9 Å, B-factor -300). For the RLC of the trailing head, the C-lobe of RLC (together with HC helix aa 809-824) and the N-lobe of RLC (together with HC helix aa 826-839) were docked separately into a segmented map of trailing myosin RLC ([Fig. S5](#)). The maps of actomyosin, ELC-centred myosin double-head and RLC-centred myosin double-head were aligned in Chimera in order to unify the

coordinate system of all models. In the end, a final homology model was calculated based on these initial models and the sequences of mouse myosin heavy chain and light chains from mouse fast muscle using SWISS-MODEL (74). In order to compare the difference of RLC-RLC interface between active and inactive myosin, this model was compared to previous structures of myosin IHM (38) (PDB: 6XE9) through aligning the leading head RLC from our model to the free head RLC from IHM in Chimera.

Sequence analysis of nebulin and troponin T

As a defined boundary on nebulin sequence between A-band and I-band is not present, the nebulin sequence of M1-8 and the entire super repeat region (Fig. 4A) from mouse (Uniprot: E9Q1W3) was considered as the A-band nebulin sequence and divided into 176 simple repeats (M1-162) through placing the SDxxYK motif at position 18-23. Multiple sequence alignment was performed using ClustalW (75) with gaps disabled (Fig. S8A) and visualised in WebLogo (76). Secondary structure of each simple repeat was predicted using RaptorX-Property (77). Probability values for being α -helix at each residue position were averaged and used for Fig. 4 and Fig. S8. To estimate relationship between the charge of the amino acid at position 15 and 21 a Bayesian multi-nominal regression was performed. For both positions and for each of the 176 sequences, the amino acid type was assigned a number, representing one of four categories which are 1 (Positive), 2 (Negative), 3 (Hydrophobic) and 4 (Other). With this, the categorical variables $y_{i,j}^{15}$ and $y_{i,j}^{21}$ were constructed, representing the category i at position 15 and 21 for sequence j respectively. The hierarchical Bayesian model was then modelled the following way and fitted with Stan (78):

$$\begin{aligned}
a_i &\sim \text{normal}(0,1) \\
\beta_i &\sim \text{normal}(-0.3,1.5) \\
y_{i,j}^{21} &= \text{softmax}\left(\alpha_i + \sum_{k=1}^4 \beta_k x_{i,j}^{15}\right) \\
p_{i,j}^{15} &= \text{cat}(y_{i,j}^{21})
\end{aligned}$$

Where a_i is the intercept, β_i the regression coefficients and $p_{i,j}^{15}$ the probability of seeing category i in sequence j . The variable $x_{i,j}^{15}$ is an indicator variable which is one when sequence j at position 15 is of class i . The priors for a_i and β_i were chosen in a way to that the prior predictive distribution of $p_{i,j}^{15}$ has mean probability for each class of 0.18. After fitting, 1000 samples were drawn from the posterior distribution for each possible state of category of amino acid 21 ([Fig. S9B](#)).

Troponin T linker sequence was from mouse fast skeletal muscle troponin T (UniProt: Q9QZ47-1) after sequence alignment with the sequence of the missing segment of troponin T (R151-S198) in PDB: 6KN8(34). Hydrophobicity score ([Fig. 6D](#)) was calculated through ProtScale (79) using the scale from Abraham & Leo (80).

References and notes

1. M. Yuen, C. A. C. Ottenheijm, Nebulin: big protein with big responsibilities. *J. Muscle Res. Cell Motil.* **41**, 103–124 (2020).
2. Z. Wang, M. Grange, T. Wagner, A. L. Kho, M. Gautel, S. Raunser, The molecular basis
5 for sarcomere organization in vertebrate skeletal muscle. *Cell.* **184**, 2135–2150.e13 (2021).
3. K. Wang, C. L. Williamson, Identification of an N2 line protein of striated muscle. *Proc. Natl. Acad. Sci. U. S. A.* **77**, 3254–3258 (1980).
4. K. Wang, J. Wright, Architecture of the sarcomere matrix of skeletal muscle:
Immunoelectron microscopic evidence that suggests a set of parallel inextensible nebulin
10 filaments anchored at the Z line. *J. Cell Biol.* **107**, 2199–2212 (1988).
5. C. T. Pappas, P. A. Krieg, C. C. Gregorio, Nebulin regulates actin filament lengths by a
stabilization mechanism. *J. Cell Biol.* **189**, 859–870 (2010).
6. N. B. Romero, S. A. Sandaradura, N. F. Clarke, Recent advances in nemaline myopathy.
Curr. Opin. Neurol. **26**, 519–526 (2013).
- 15 7. C. A. Sewry, J. M. Laitila, C. Wallgren-Pettersson, Nemaline myopathies: a current view.
J. Muscle Res. Cell Motil. **40**, 111–126 (2019).
8. M. M. Ryan, C. Schnell, C. D. Strickland, L. K. Shield, G. Morgan, S. T. Iannaccone, N.
G. Laing, A. H. Beggs, K. N. North, Nemaline myopathy: A clinical study of 143 cases.
Ann. Neurol. **50**, 312–320 (2001).
- 20 9. C. L. Moncman, K. Wang, Nebulette: A 107 kD nebulin-like protein in cardiac muscle.
Cell Motil. Cytoskeleton. **32**, 205–225 (1995).
10. T. Burgoyne, F. Muhamad, P. K. Luther, Visualization of cardiac muscle thin filaments
and measurement of their lengths by electron tomography. *Cardiovasc. Res.* **77**, 707–712
(2008).

11. J. Kolb, F. Li, M. Methawasin, M. Adler, Y. N. Escobar, J. Nedrud, C. T. Pappas, S. P. Harris, H. Granzier, Thin filament length in the cardiac sarcomere varies with sarcomere length but is independent of titin and nebulin. *J. Mol. Cell. Cardiol.* **97**, 286–294 (2016).
12. S. Labeit, B. Kolmerer, The Complete Primary Structure of Human Nebulin and its
5 Correlation to Muscle Structure. *Mol. Biol.*, 308–315 (1995).
13. K. Donner, M. Sandbacka, V. L. Lehtokari, C. Wallgren-Pettersson, K. Pelin, Complete genomic structure of the human nebulin gene and identification of alternatively spliced transcripts. *Eur. J. Hum. Genet.* **12**, 744–751 (2004).
14. A. S. McElhinny, B. Kolmerer, V. M. Fowler, S. Labeit, C. C. Gregorio, The N-terminal
10 end of nebulin interacts with tropomodulin at the pointed ends of the thin filaments. *J. Biol. Chem.* **276**, 583–592 (2001).
15. C. T. Pappas, N. Bhattacharya, J. A. Cooper, C. C. Gregorio, Nebulin Interacts with CapZ and Regulates Thin Filament Architecture within the Z-Disc. *Mol. Biol. Cell.* **19**, 1837–1847 (2008).
16. S. Labeit, T. Gibson, A. Lakey, K. Leonard, M. Zeviani, P. Knight, J. Wardale, J. Trinick,
15 Evidence that nebulin is a protein-ruler in muscle thin filaments. *FEBS Lett.* **282**, 313–316 (1991).
17. D. S. Gokhin, N. E. Kim, S. A. Lewis, H. R. Hoenecke, D. D. D’Lima, V. M. Fowler,
20 Thin-filament length correlates with fiber type in human skeletal muscle. *Am. J. Physiol. - Cell Physiol.* **302**, 555–565 (2012).
18. B. Kiss, J. Gohlke, P. Tonino, Z. Hourani, J. Kolb, J. Strom, O. Alekhina, J. E. Smith, C. Ottenheijm, C. Gregorio, H. Granzier, Nebulin and Lmod2 are critical for specifying thin-filament length in skeletal muscle. *Sci. Adv.* **6**, 1–18 (2020).
19. V. M. Fowler, C. R. McKeown, R. S. Fischer, Nebulin: Does It Measure up as a Ruler?

Curr. Biol. **16**, 18–20 (2006).

20. C. C. Witt, C. Burkart, D. Labeit, M. McNabb, Y. Wu, H. Granzier, S. Labeit, Nebulin regulates thin filament length, contractility, and Z-disk structure in vivo. *EMBO J.* **25**, 3843–3855 (2006).
- 5 21. M. L. Bang, X. Li, R. Littlefield, S. Bremner, A. Thor, K. U. Knowlton, R. L. Lieber, J. Chen, Nebulin-deficient mice exhibit shorter thin filament lengths and reduced contractile function in skeletal muscle. *J. Cell Biol.* **173**, 905–916 (2006).
22. S. M. Gonsior, M. Gautel, H. Hinssen, A six-module human nebulin fragment bundles actin filaments and induces actin polymerization. *J. Muscle Res. Cell Motil.* **19**, 225–235
10 (1998).
23. M. Pfuhl, S. J. Winder, A. Pastore, Nebulin, a helical actin binding protein. *EMBO J.* **13**, 1782–1789 (1994).
24. S. Pospich, F. Merino, S. Raunser, Structural Effects and Functional Implications of Phalloidin and Jasplakinolide Binding to Actin Filaments. *Structure.* **28**, 437-449.e5
15 (2020).
25. X. Ao, S. S. Lehrer, Phalloidin unzips nebulin from thin filaments in skeletal myofibrils. *J. Cell Sci.* **108**, 3397–3403 (1995).
26. A. Castillo, R. Nowak, K. P. Littlefield, V. M. Fowler, R. S. Littlefield, A nebulin ruler does not dictate thin filament lengths. *Biophys. J.* **96**, 1856–1865 (2009).
- 20 27. N. Lukoyanova, M. S. VanLoock, A. Orlova, V. E. Galkin, K. Wang, E. H. Egelman, Each actin subunit has three nebulin binding sites: Implications for steric blocking. *Curr. Biol.* **12**, 383–388 (2002).
28. K. J. V. Poole, M. Lorenz, G. Evans, G. Rosenbaum, A. Pirani, R. Craig, L. S. Tobacman, W. Lehman, K. C. Holmes, A comparison of muscle thin filament models obtained from

electron microscopy reconstructions and low-angle X-ray fibre diagrams from non-overlap muscle. *J. Struct. Biol.* **155**, 273–284 (2006).

29. M. Marttila, M. Hanif, E. Lemola, K. J. Nowak, J. Laitila, M. Grönholm, C. Wallgren-Pettersson, K. Pelin, Nebulin interactions with actin and tropomyosin are altered by disease-causing mutations. *Skelet. Muscle.* **4**, 1–10 (2014).
30. J. Q. Zhang, A. Weisberg, R. Horowitz, Expression and purification of large nebulin fragments and their interaction with actin. *Biophys. J.* **74**, 349–359 (1998).
31. R. Chitose, A. Watanabe, M. Asano, A. Hanashima, K. Sasano, Y. Bao, K. Maruyama, S. Kimura, Isolation of nebulin from rabbit skeletal muscle and its interaction with actin. *J. Biomed. Biotechnol.* **2010** (2010), doi:10.1155/2010/108495.
32. J. Jumper, R. Evans, A. Pritzel, T. Green, M. Figurnov, O. Ronneberger, K. Tunyasuvunakool, R. Bates, A. Žídek, A. Potapenko, A. Bridgland, C. Meyer, S. A. A. Kohl, A. J. Ballard, A. Cowie, B. Romera-Paredes, S. Nikolov, R. Jain, J. Adler, T. Back, S. Petersen, D. Reiman, E. Clancy, M. Zielinski, M. Steinegger, M. Pacholska, T. Berghammer, S. Bodenstein, D. Silver, O. Vinyals, A. W. Senior, K. Kavukcuoglu, P. Kohli, D. Hassabis, Highly accurate protein structure prediction with AlphaFold. *Nature* (2021), doi:10.1038/s41586-021-03819-2.
33. M.-L. Bang, M. Caremani, E. Brunello, R. Littlefield, R. L. Lieber, J. Chen, V. Lombardi, M. Linari, Nebulin plays a direct role in promoting strong actin-myosin interactions. *FASEB J.* **23**, 4117–4125 (2009).
34. M. Chandra, R. Manidi, S. Ford, C. Hidalgo, C. Witt, C. Ottenheijm, S. Labeit, H. Granzier, Nebulin alters cross-bridge cycling kinetics and increases thin filament activation. A novel mechanism for increasing tension and reducing tension cost. *J. Biol. Chem.* **284**, 30889–30896 (2009).

35. B. Kiss, E. J. Lee, W. Ma, F. W. Li, P. Tonino, S. M. Mijailovich, T. C. Irving, H. L. Granzier, Nebulin stiffens the thin filament and augments cross-bridge interaction in skeletal muscle. *Proc. Natl. Acad. Sci. U. S. A.* **115**, 10369–10374 (2018).
36. J. P. Jin, K. Wang, Cloning, expression, and protein interaction of human nebulin fragments composed of varying numbers of sequence modules. *J. Biol. Chem.* **266**, 21215–21223 (1991).
37. D. D. Root, K. Wang, Calmodulin-Sensitive Interaction of Human Nebulin Fragments with Actin and Myosin. *Biochemistry*, 12581–12591 (1994).
38. S. Yang, P. Tiwari, K. H. Lee, O. Sato, M. Ikebe, R. Padrón, R. Craig, Cryo-EM structure of the inhibited (10S) form of myosin II. *Nature*. **588**, 521–525 (2020).
39. C. A. Scarff, G. Carrington, D. Casas-Mao, J. M. Chalovich, P. J. Knight, N. A. Ranson, M. Peckham, Structure of the shutdown state of myosin-2. *Nature*. **588**, 515–520 (2020).
40. M. Kruger, J. Wright, K. Wang, Nebulin as a length regulator of thin filaments of vertebrate skeletal muscles: Correlation of thin filament length, nebulin size, and epitope profile. *J. Cell Biol.* **115**, 97–107 (1991).
41. E. P. Manning, J. C. Tardiff, S. D. Schwartz, A model of calcium activation of the cardiac thin filament. *Biochemistry*. **50**, 7405–7413 (2011).
42. Y. Yamada, K. Namba, T. Fujii, Cardiac muscle thin filament structures reveal calcium regulatory mechanism. *Nat. Commun.* **11**, 1–3 (2020).
43. C. M. Risi, I. Pepper, B. Belknap, M. Landim-Vieira, H. D. White, K. Dryden, J. R. Pinto, P. B. Chase, V. E. Galkin, The structure of the native cardiac thin filament at systolic Ca²⁺ levels. *Proc. Natl. Acad. Sci. U. S. A.* **118**, 2–9 (2021).
44. J. J. Johnston, R. I. Kelley, T. O. Crawford, D. H. Morton, R. Agarwala, T. Koch, A. A. Schäffer, C. A. Francomano, L. G. Biesecker, A novel nemaline myopathy in the Amish

caused by a mutation in troponin T1. *Am. J. Hum. Genet.* **67**, 814–821 (2000).

45. S. A. Sandaradura, A. Bournazos, A. Mallawaarachchi, B. B. Cummings, L. B. Waddell, K. J. Jones, C. Troedson, A. Sudarsanam, B. M. Nash, G. B. Peters, E. M. Algar, D. G. MacArthur, K. N. North, S. Brammah, A. Charlton, N. G. Laing, M. J. Wilson, M. R. Davis, S. T. Cooper, Nemaline myopathy and distal arthrogryposis associated with an autosomal recessive TNNT3 splice variant. *Hum. Mutat.* **39**, 383–388 (2018).

46. S. T. Kazmierski, P. B. Antin, C. C. Witt, N. Huebner, A. S. McElhinny, S. Labeit, C. C. Gregorio, The complete mouse nebulin gene sequence and the identification of cardiac nebulin. *J. Mol. Biol.* **328**, 835–846 (2003).

47. V. L. Lehtokari, K. Kiiski, S. A. Sandaradura, J. Laporte, P. Repo, J. A. Frey, K. Donner, M. Marttila, C. Saunders, P. G. Barth, J. T. den Dunnen, A. H. Beggs, N. F. Clarke, K. N. North, N. G. Laing, N. B. Romero, T. L. Winder, K. Pelin, C. Wallgren-Pettersson, Mutation update: The spectra of nebulin variants and associated myopathies. *Hum. Mutat.* **35**, 1418–1426 (2014).

48. F. J. O'Reilly, L. Xue, A. Graziadei, L. Sinn, S. Lenz, D. Tegunov, C. Blötz, N. Singh, W. J. H. Hagen, P. Cramer, J. Stülke, J. Mahamid, J. Rappsilber, In-cell architecture of an actively transcribing-translating expressome. *Science (80-.)*. **369**, 554–557 (2020).

49. R. J. Solaro, D. C. Pang, F. N. Briggs, The purification of cardiac myofibrils with Triton X-100. *BBA - Bioenerg.* **245**, 259–262 (1971).

50. S. Tacke, P. Erdmann, Z. Wang, S. Klumpe, M. Grange, J. Plitzko, S. Raunser, A streamlined workflow for automated cryo focused ion beam milling. *J. Struct. Biol.*, 107743 (2021).

51. D. N. Mastronarde, Automated electron microscope tomography using robust prediction of specimen movements. *J. Struct. Biol.* **152**, 36–51 (2005).

52. Y. Yang, S. Gourinath, M. Kovács, L. Nyitray, R. Reutzel, D. M. Himmel, E. O'Neill-Hennessey, L. Reshetnikova, A. G. Szent-Györgyi, J. H. Brown, C. Cohen, Rigor-like Structures from Muscle Myosins Reveal Key Mechanical Elements in the Transduction Pathways of This Allosteric Motor. *Structure*. **15**, 553–564 (2007).
53. W. J. H. Hagen, W. Wan, J. A. G. Briggs, Implementation of a cryo-electron tomography tilt-scheme optimized for high resolution subtomogram averaging. *J. Struct. Biol.* **197**, 191–198 (2017).
54. S. Q. Zheng, E. Palovcak, J. P. Armache, K. A. Verba, Y. Cheng, D. A. Agard, MotionCor2: Anisotropic correction of beam-induced motion for improved cryo-electron microscopy. *Nat. Methods*. **14**, 331–332 (2017).
55. J. R. Kremer, D. N. Mastronarde, J. R. McIntosh, Computer visualization of three-dimensional image data using IMOD. *J. Struct. Biol.* **116**, 71–76 (1996).
56. J. Y. Tinevez, N. Perry, J. Schindelin, G. M. Hoopes, G. D. Reynolds, E. Laplantine, S. Y. Bednarek, S. L. Shorte, K. W. Eliceiri, TrackMate: An open and extensible platform for single-particle tracking. *Methods*. **115**, 80–90 (2017).
57. J. Schindelin, I. Arganda-Carreras, E. Frise, V. Kaynig, M. Longair, T. Pietzsch, S. Preibisch, C. Rueden, S. Saalfeld, B. Schmid, J. Y. Tinevez, D. J. White, V. Hartenstein, K. Eliceiri, P. Tomancak, A. Cardona, Fiji: An open-source platform for biological-image analysis. *Nat. Methods*. **9**, 676–682 (2012).
58. C. A. Schneider, W. S. Rasband, K. W. Eliceiri, NIH Image to ImageJ: 25 years of image analysis. *Nat. Methods*. **9**, 671–675 (2012).
59. T. Wagner, F. Merino, M. Stabrin, T. Moriya, C. Antoni, A. Apelbaum, P. Hagel, O. Sitsel, T. Raisch, D. Prumbaum, D. Quentin, D. Roderer, S. Tacke, B. Siebolds, E. Schubert, T. R. Shaikh, P. Lill, C. Gatsogiannis, S. Raunser, SPHIRE-crYOLO is a fast

and accurate fully automated particle picker for cryo-EM. *Commun. Biol.* **2**, 1–13 (2019).

60. T. A. M. Bharat, S. H. W. Scheres, Resolving macromolecular structures from electron cryo-Tomography data using subtomogram averaging in RELION. *Nat. Protoc.* **11**, 2054–2065 (2016).

5 61. Z. Yang, J. Fang, J. Chittuluru, F. J. Asturias, P. A. Penczek, Iterative stable alignment and clustering of 2D transmission electron microscope images. *Structure.* **20**, 237–247 (2012).

62. D. Tegunov, L. Xue, C. Dienemann, P. Cramer, J. Mahamid, Multi-particle cryo-EM refinement with M visualizes ribosome-antibiotic complex at 3.5 Å in cells. *Nat. Methods.* **18**, 186–193 (2021).

10

63. D. Tegunov, P. Cramer, Real-time cryo-electron microscopy data preprocessing with Warp. *Nat. Methods.* **16**, 1146–1152 (2019).

64. T. Moriya, M. Saur, M. Stabrin, F. Merino, H. Voicu, Z. Huang, P. A. Penczek, S. Raunser, C. Gatsogiannis, High-resolution single particle analysis from electron cryo-microscopy images using SPHIRE. *J. Vis. Exp.* **2017**, 1–11 (2017).

15

65. T. C. Terwilliger, S. J. Ludtke, R. J. Read, P. D. Adams, P. V. Afonine, Improvement of cryo-EM maps by density modification. *Nat. Methods.* **17**, 923–927 (2020).

66. N. Eswar, D. Eramian, B. Webb, M.-Y. Shen, A. Sali, in *Structural Proteomics: High-Throughput Methods*, B. Kobe, M. Guss, T. Huber, Eds. (Humana Press, Totowa, NJ, 2008; https://doi.org/10.1007/978-1-60327-058-8_8), pp. 145–159.

20

67. J. von der Ecken, S. M. Heissler, S. Pathan-Chhatbar, D. J. Manstein, S. Raunser, Cryo-EM structure of a human cytoplasmic actomyosin complex at near-atomic resolution. *Nature.* **534**, 724–728 (2016).

68. P. Emsley, B. Lohkamp, W. G. Scott, K. Cowtan, Features and development of Coot. *Acta*

Crystallogr. Sect. D Biol. Crystallogr. **66**, 486–501 (2010).

69. T. I. Croll, ISOLDE: a physically realistic environment for model building into low-resolution electron-density maps. *Acta Crystallogr. Sect. D.* **74**, 519–530 (2018).

70. T. D. Goddard, C. C. Huang, E. C. Meng, E. F. Pettersen, G. S. Couch, J. H. Morris, T. E. Ferrin, UCSF ChimeraX: Meeting modern challenges in visualization and analysis. *Protein Sci.* **27**, 14–25 (2018).

71. P. V Afonine, B. P. Klaholz, N. W. Moriarty, B. K. Poon, O. V Sobolev, T. C. Terwilliger, P. D. Adams, A. Urzhumtsev, New tools for the analysis and validation of cryo-EM maps and atomic models. *Acta Crystallogr. Sect. D.* **74**, 814–840 (2018).

72. V. B. Chen, W. B. Arendall III, J. J. Headd, D. A. Keedy, R. M. Immormino, G. J. Kapral, L. W. Murray, J. S. Richardson, D. C. Richardson, MolProbity: all-atom structure validation for macromolecular crystallography. *Acta Crystallogr. Sect. D.* **66**, 12–21 (2010).

73. B. A. Barad, N. Echols, R. Y. R. Wang, Y. Cheng, F. Dimaio, P. D. Adams, J. S. Fraser, EMRinger: Side chain-directed model and map validation for 3D cryo-electron microscopy. *Nat. Methods.* **12**, 943–946 (2015).

74. A. Waterhouse, M. Bertoni, S. Bienert, G. Studer, G. Tauriello, R. Gumienny, F. T. Heer, T. A. P. De Beer, C. Rempfer, L. Bordoli, R. Lepore, T. Schwede, SWISS-MODEL: Homology modelling of protein structures and complexes. *Nucleic Acids Res.* **46**, W296–W303 (2018).

75. M. A. Larkin, G. Blackshields, N. P. Brown, R. Chenna, P. A. Mcgettigan, H. McWilliam, F. Valentin, I. M. Wallace, A. Wilm, R. Lopez, J. D. Thompson, T. J. Gibson, D. G. Higgins, Clustal W and Clustal X version 2.0. *Bioinformatics.* **23**, 2947–2948 (2007).

76. G. E. Crooks, G. Hon, J. M. Chandonia, S. E. Brenner, WebLogo: A sequence logo

generator. *Genome Res.* **14**, 1188–1190 (2004).

77. S. Wang, W. Li, S. Liu, J. Xu, RaptorX-Property: a web server for protein structure property prediction. *Nucleic Acids Res.* **44**, W430–W435 (2016).
78. Stan Development Team. Stan Modeling Language Users Guide and Reference Manual, 2.27 (2019). <https://mc-stan.org>
79. E. Gasteiger, C. Hoogland, A. Gattiker, S. Duvaud, M. R. Wilkins, R. D. Appel, A. Bairoch, in *The Proteomics Protocols Handbook*, J. M. Walker, Ed. (Humana Press, Totowa, NJ, 2005; <https://doi.org/10.1385/1-59259-890-0:571>), pp. 571–607.
80. D. J. Abraham, A. J. Leo, Extension of the fragment method to calculate amino acid zwitterion and side chain partition coefficients. *Proteins Struct. Funct. Bioinforma.* **2**, 130–152 (1987).

Acknowledgements: We thank S. Tacke for hardware optimisation for cryo-FIB. We are grateful to O. Hofnagel and D. Prumbaum for EM support and B. Brandmeier for technical support. We thank S. Biswas for support in manual particle selection.

5 **Funding:** This work was supported by funds from the Max Planck Society (to S.R.), the Wellcome Trust (Collaborative Award in Sciences 201543/Z/16/Z to S.R. and M. Gautel), the European Research Council under the European Union's Horizon 2020 Programme (ERC-2019-SyG, grant no. 856118 to S.R. and M. Gautel) and the Medical Research Council (MR/R003106/1 to M. Gautel and A.L.K.). M. Grange was supported by an EMBO Long-Term Fellowship. M. Gautel
10 holds the BHF Chair of Molecular Cardiology.

Author contributions: S.R. designed and supervised the project. A.L.K. and M. Gautel developed methods and isolated mouse myofibrils. Z.W. performed cryo-FIB and collected cryo-ET data. M. Grange optimised cryo-ET data acquisition. Z.W. and M. Grange performed sub-tomogram
15 averaging. T.W. implemented automatic filament picking and tools for data conversion and statistical analysis. S.P. built atomic models for actin, nebulin and myosin motor domain. Z.W. performed rigid body fitting of myosin neck domain models. Z.W. prepared figures with the assistance of M. Grange. Z.W., M. Grange, M. Gautel and S.R. wrote the manuscript. All authors reviewed the results and commented on the manuscript.

20 **Competing interests:** The authors declare no competing interests.

Data and materials availability:

Cryo-ET structures are deposited in the Electron Microscopy Data Bank under accession numbers EMD-13990 (skeletal A-band actin-nebulin), EMD-13991 (skeletal actomyosin), EMD-13992 (skeletal ELC-centred myosin), EMD-13993 (skeletal RLC-centred myosin), EMD-13994 (skeletal I-band actin-nebulin), EMD-13995 (cardiac actin), EMD-13996 (cardiac actomyosin), EMD-13997 (cardiac myosin neck domain). Representative tomograms are deposited under accession numbers EMD-13998 (skeletal A-band), EMD-13999 (skeletal I-band), EMD-14000 (cardiac A-band). The atomic models are deposited in Protein Data Bank under accession numbers 7QIM (skeletal actin-nebulin), 7QIN (skeletal actomyosin) and 7QIO (skeletal myosin neck domain). Other structures and EM density maps used in this study are available in PDB: 3I5G, 6KN8, 6XE9 and in EMDB: EMD-0729.

Supplementary Materials

Figs. S1 to S11

Table S1

Movies S1 to S4

Figure legends

Fig. 1 Thin filament structures in striated muscle sarcomeres. (A) Tomographic slice of skeletal sarcomere A-band depicting adjacent thin and thick filaments. (B) Actomyosin structure from the skeletal sarcomere A-band consisting of actin (green), myosin (heavy chain (HC): yellow, essential light chain (ELC): orange, regulatory light chain (RLC): red), tropomyosin (blue) and nebulin (magenta). Myosin is a composite map including light chains from different averaged structures (see [Figs. S1,S5](#)). Cross-section view of the structure is shown in the inset. (C) Different components of a thin filament and their position highlighted within the structure. The dotted line highlights the interface between the two RLCs of the trailing and leading myosin head. (D) Tomographic slice of a skeletal sarcomere I-band and structure of the thin filament (inset). (E) Tomographic slice of a cardiac sarcomere A-band and structure of actomyosin, including a pair of myosin double-heads. All tomographic slices are 7 nm thick. Scale bars: 20 nm

Fig. 2 Actin in a thin filament and different tropomyosin states on a thin filament. (A) Helical parameters of F-actin determined within a thin filament in a sarcomere. (B) Comparison of the structures of actin subunit from different filamentous structures. (C-E) Different views depicting a thin filament including nebulin and different states of tropomyosin. (F) Zoom-in view of nebulin, tropomyosin and actin depicting the physical separation between nebulin and tropomyosin by the SD3 and 4 of actin subunits.

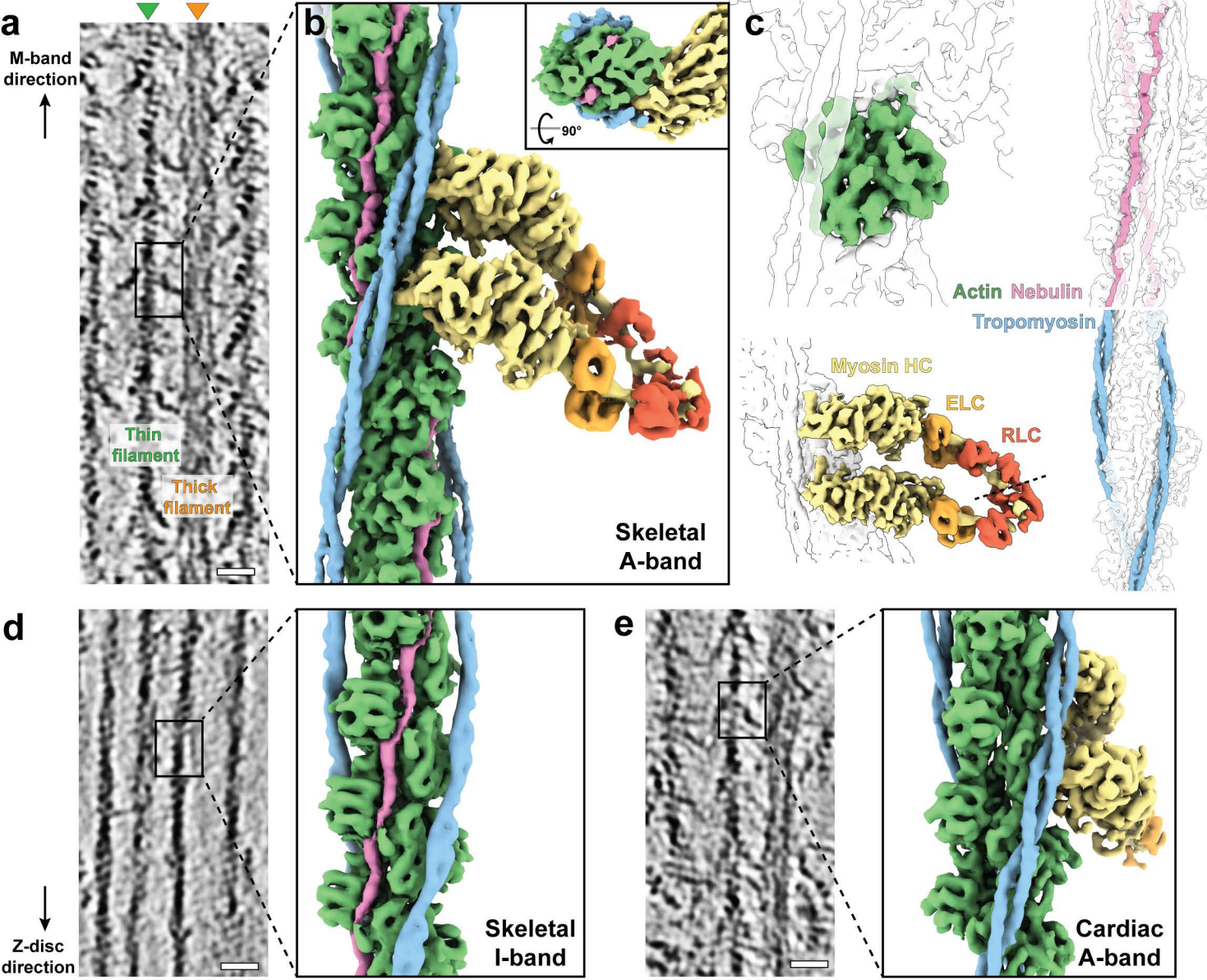
Fig. 3 Structural variability within the in situ myosin double-head in skeletal muscle. (A) The lever arms of the trailing and leading myosin heads form kinked helices (yellow). Different angles at the kinks between the two heads are labelled. ELCs and RLCs are shown as transparent models. (B) Different conformations of the lever arm at the RLC-binding regions of the trailing head (purple) and the leading head (green). (C) View from the eye symbol in (A) showing the interface between the RLCs from the trailing and leading head (red for RLC, yellow for lever arm helices) compared to the interface of the blocked head (aligned to the leading head) and the free head in the IHM (blue for RLC, dark blue for lever arm helices). (D) Two different conformations, straight and bent forms, of myosin double heads determined by 3D classification. HC, ELC and RLC regions are coloured in yellow, orange and red. (E) Comparison between the straight (orange) and bent (purple) double-head conformation. The origin of bending is marked by an asterisk, also in (A). (F) Schematic drawing describing the increased range of thin filament positions that can be bound by myosin heads due to the bending of double-head. (G) Schematic drawing depicting the three flexible junctions in a myosin head.

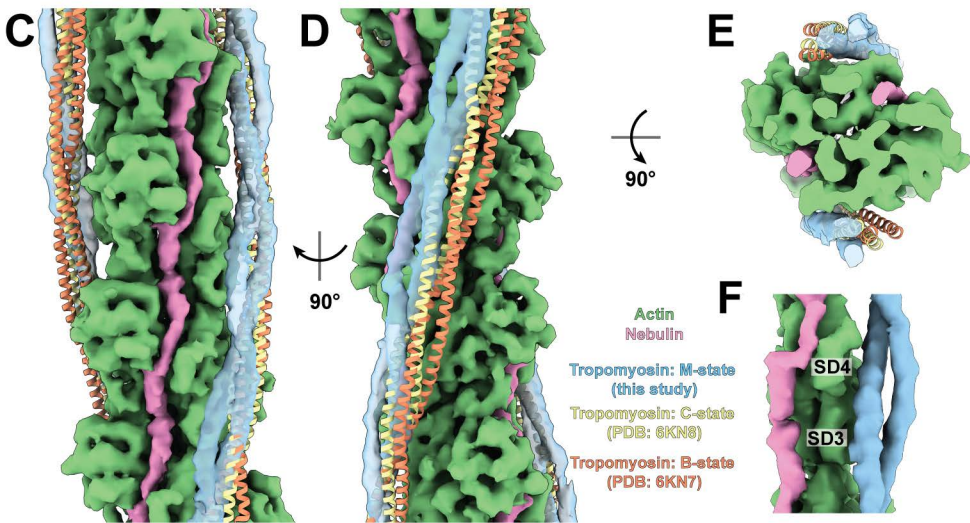
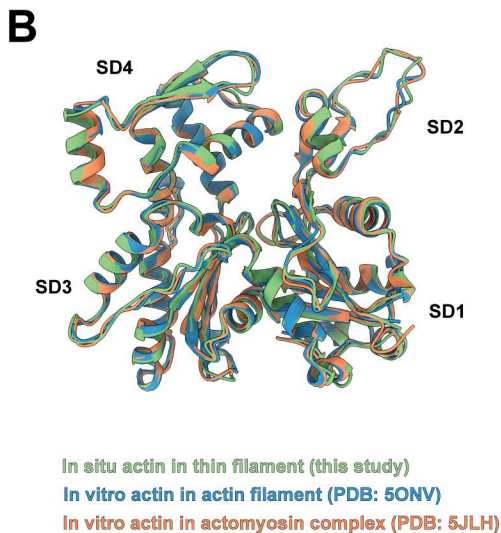
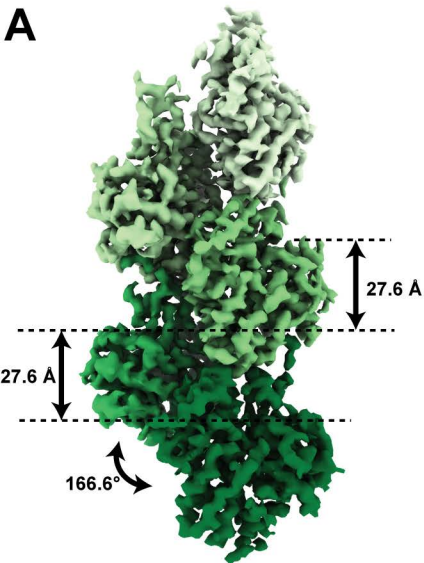
Fig. 4 Nebulin structure and its binding to the actin filament. (A) Schematic drawing of the nebulin-bound thin filament. (B) Modular organisation of the primary sequence of nebulin demonstrating its super repeats and simple repeats. Nebulin contains an N-terminal sequence (orange), repeats 1-8 (M1-M8, bright magenta), a super repeat region (magenta), repeat 163-185 (M163-M185, blue), a serine-rich region (Ser, green) and a C-terminal Src homology-3 domain (SH3, purple). The number below each simple repeat indicates its most common size, in number of amino acids. (C) Sub-tomogram averaged structure of the actin filament in complex with nebulin (magenta) at a resolution of 4.5 Å. Different actin subunits are coloured in different shades of green with darker green towards the barbed end. (D) Rotated view of (C) highlighting both

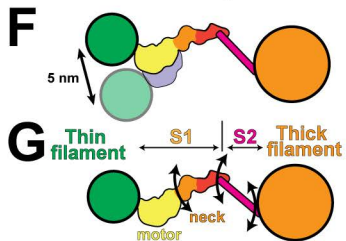
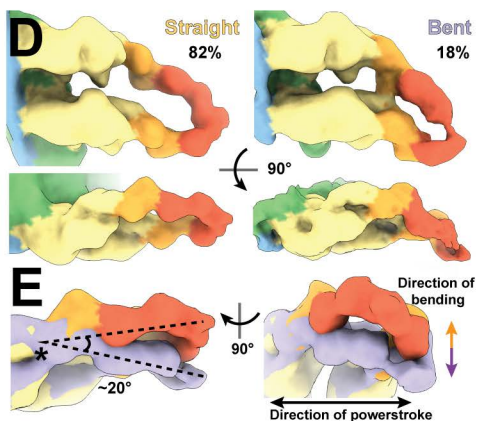
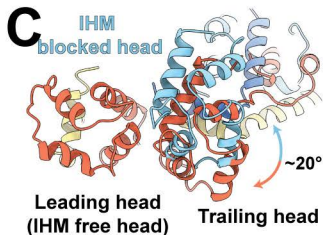
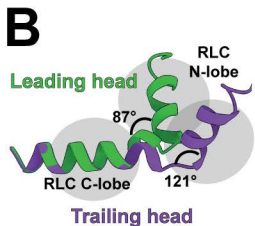
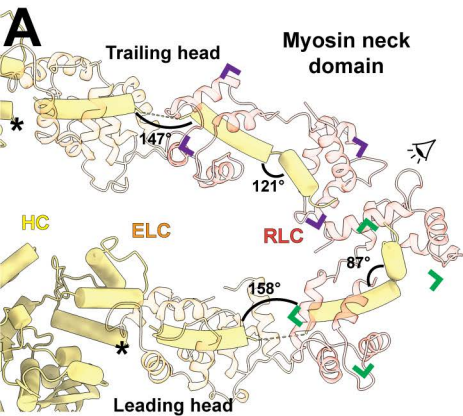
nebulin molecules (shown as structural models of three and two simple repeats) on the actin filament. Only one strand of the actin filament is shown. Nebulin simple repeats are labelled on one strand to show 1:1 stoichiometry with actin subunits. **(E)** Structural model of one actin subunit and two nebulin molecules. One nebulin binds along actin subdomain 1 and 2 (SD1 and SD2) while the other binds along actin subdomain 3 and 4 (SD3 and SD4). The cryo-EM map of the neighbouring actin subunits is shown. **(F)** Zoom-in view of one nebulin simple repeat. The side chain of residue Y22 is highlighted. **(G)** Averaged predicted score for an α -helix at each residue position of a simple repeat. **(H)** Graphical representation of sequence alignment of all simple repeats (M1-M163). A larger amino acid symbol corresponds to a greater occurrence at a certain position. Positive, negative and neutral residues are coloured in blue, red and green, respectively. Dotted lines map the sequence to the structural model in (F) and (G). Asterisks mark the conserved SDxxYK motif.

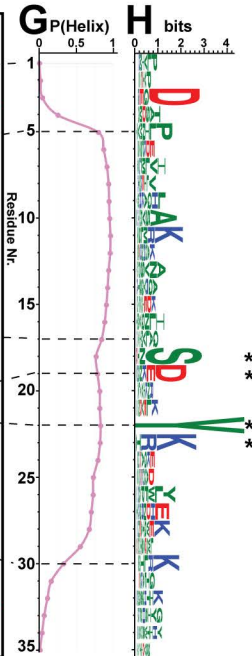
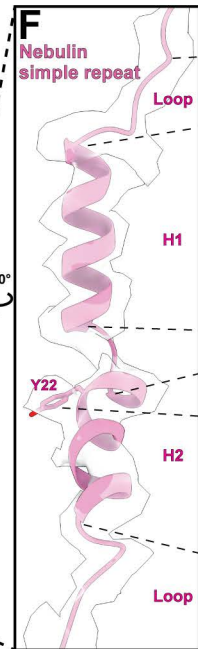
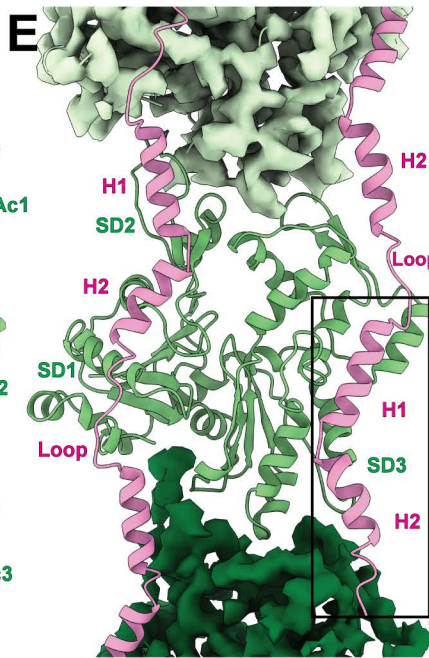
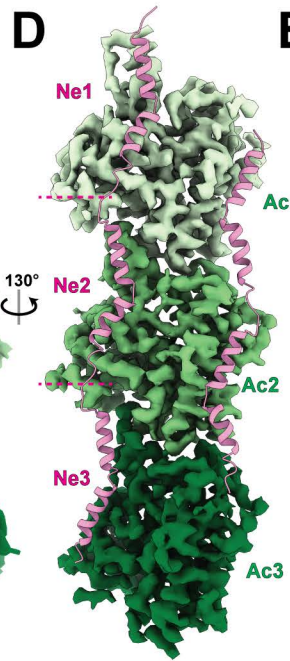
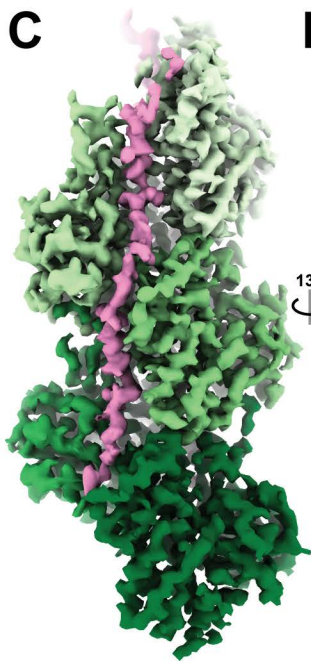
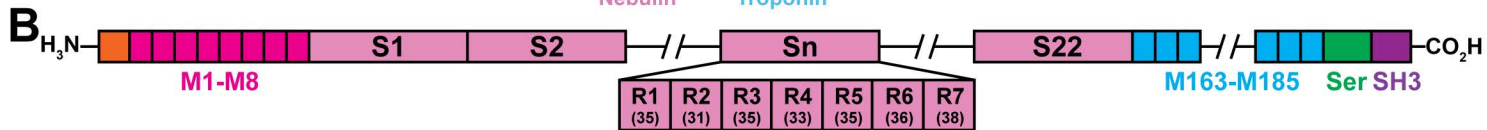
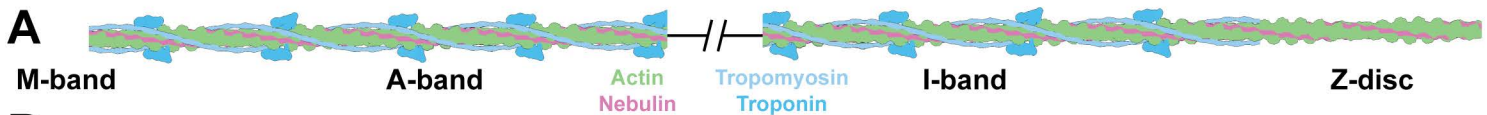
Fig. 5 Interactions between nebulin and actin. **(A)** Schematic depiction of interactions between nebulin (magenta) and three adjacent actin (green) subunits. Interactions are marked as dotted lines. **(B)** Intra-nebulin interactions (iii in (A)) between residues with complementary charges at position 15 and 21. **(C)** Details of interactions i-vii in (A). Distances were measured between actin residues and the C β of the poly-alanine model of nebulin where side chain is not resolved. A potential side chain conformation of S18 is shown for visualisation although it was not determined from the map.

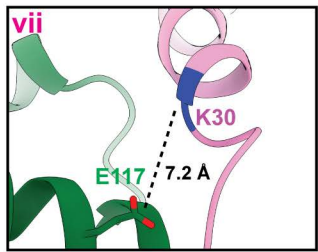
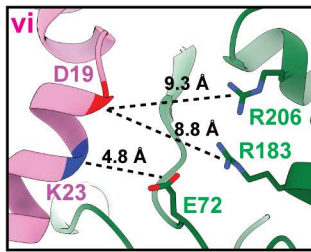
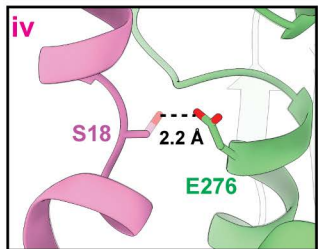
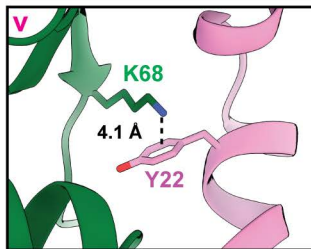
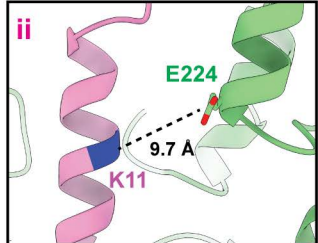
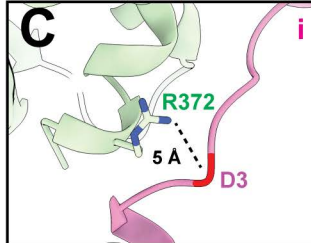
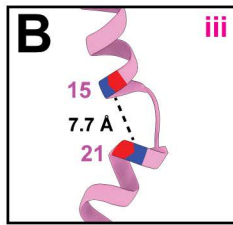
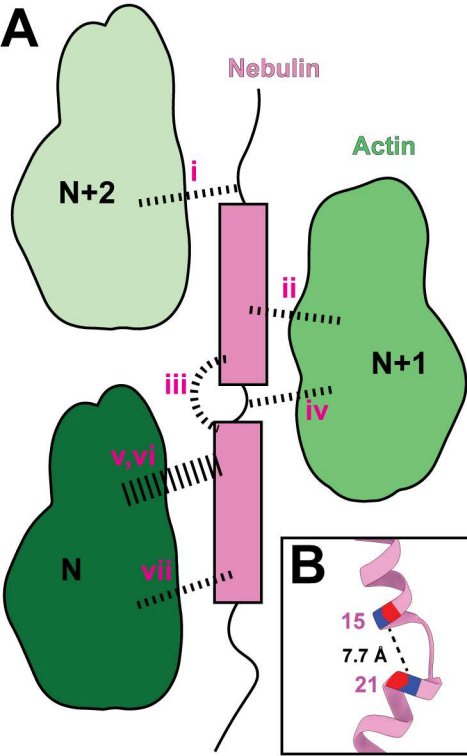
Fig. 6 Potential interactions between nebulin and troponin T (TnT). **(A).** The actin-nebulin complex superimposed with the cryo-EM densities of the troponin complex (EMD-0729). Two contact sites between nebulin and troponin T are marked in yellow as I and II. **(B)** Graphical representation of the sequence alignment of all nebulin super repeats (each super repeat contains the simple repeats R1-R7). A larger amino acid symbol corresponds to a greater occurrence at a certain position. The troponin binding sites I and II are marked corresponding to the WLKGIGW and ExxK motif. **(C)** Two different TnT models (dark blue) that bind to opposite sides of the actin filament (PDB: 6KN8) are shown. The linker region between R134 and R179 (corresponding to R151 and S198 in the original model) is missing in the structural model. Possible shapes of the TnT linkers are marked as cyan dotted lines based on weak EM densities (EMD-0729). Potential TnT binding sites on nebulin are highlighted in yellow. Tropomyosin (Tm) is shown in light blue. **(D)** Hydrophobicity of the linker in mouse fast muscle troponin T (TNNT3). Potential regions that can bind to site I and II are marked.

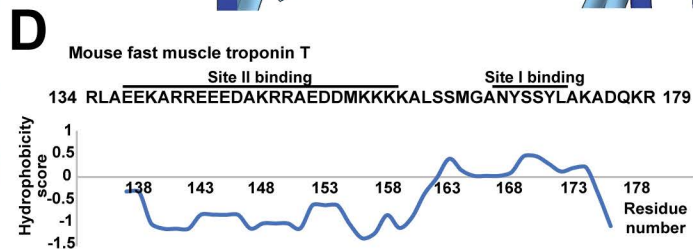
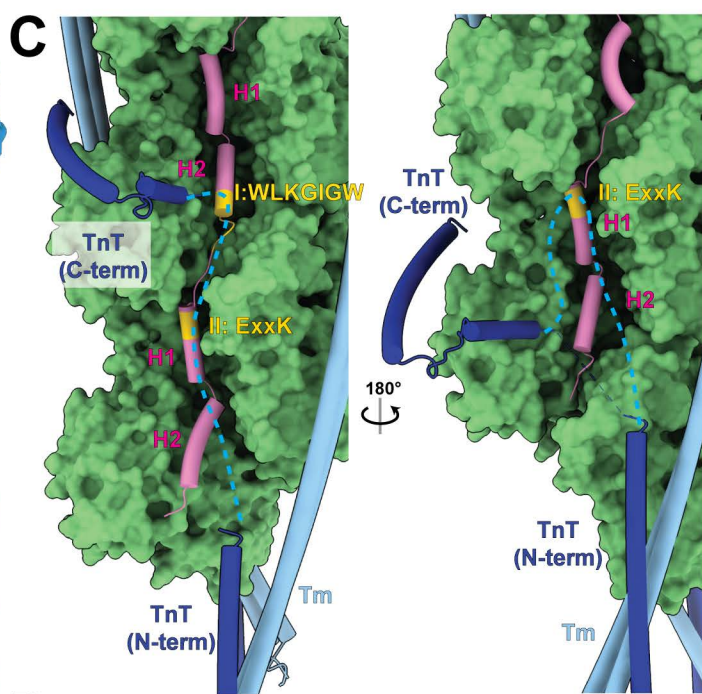
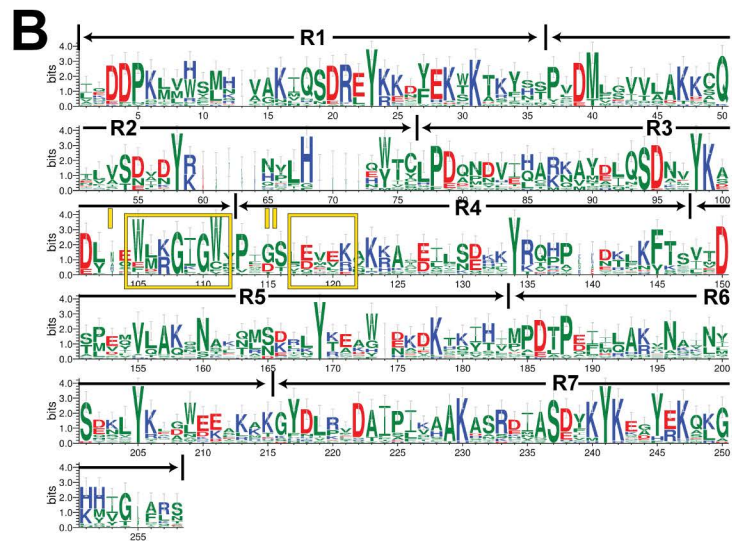
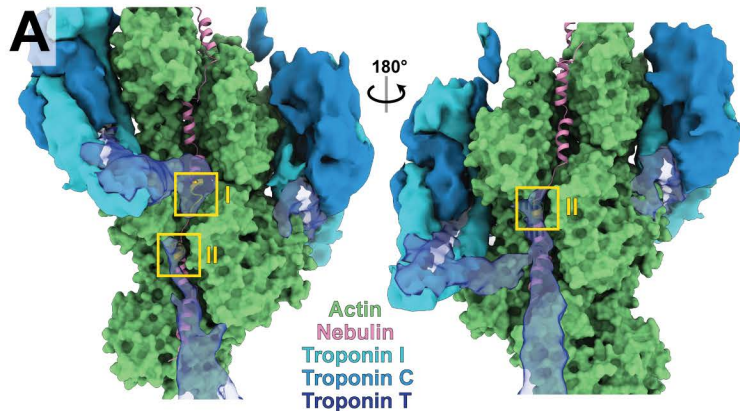














Supplementary Materials for

Structures from intact myofibrils reveal mechanism of thin filament regulation through nebulin

Zhexin Wang, Michael Grange, Sabrina Pospich, Thorsten Wagner, Ay Lin Kho, Mathias Gautel, Stefan Raunser

Correspondence to: stefan.raunser@mpi-dortmund.mpg.de

This PDF file includes:

Figs. S1 to S11
Table S1
Captions for Movies S1 to S4

Other Supplementary Materials for this manuscript include the following:

Movies S1 to S4

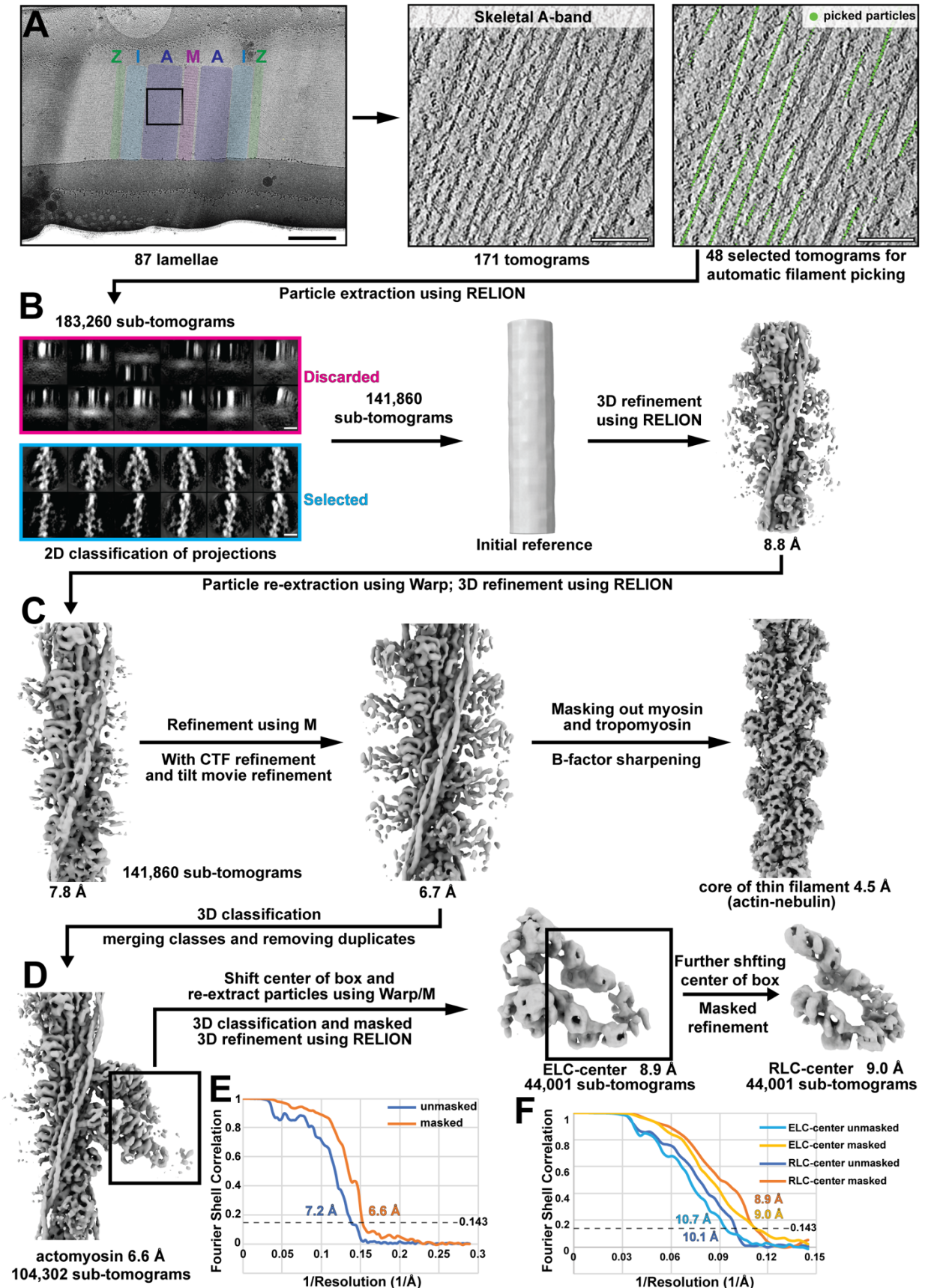


Fig. S1. Cryo-FIB-ET and processing workflow of A-band thin filament structures from mouse psoas muscle. (A) Examples of a lamella of mouse psoas myofibrils and a slice of tomogram depicting the sarcomeric A-band, where the thin filaments are picked automatically. Different zones (Z-disc, I-band, A-band, M-band) of a sarcomere on the lamella are highlighted in different colours. Scale bars: 1 μm (left), 100 nm (right). (B) Cleaning of particles using 2D classification of projection images and initial refinement using RELION. Scale bar: 10 nm. (C) Improving the resolution of the thin filament structure using the Warp-M packages. (D) Actomyosin structure (including a thin filament and two myosin heads) and structures of the myosin neck domain obtained through further classification and re-centring of particle boxes. (E) Gold-standard FSC curve of the actomyosin complex. (F) Gold-standard FSC curve of the ELC and RLC centred myosin double head structures.

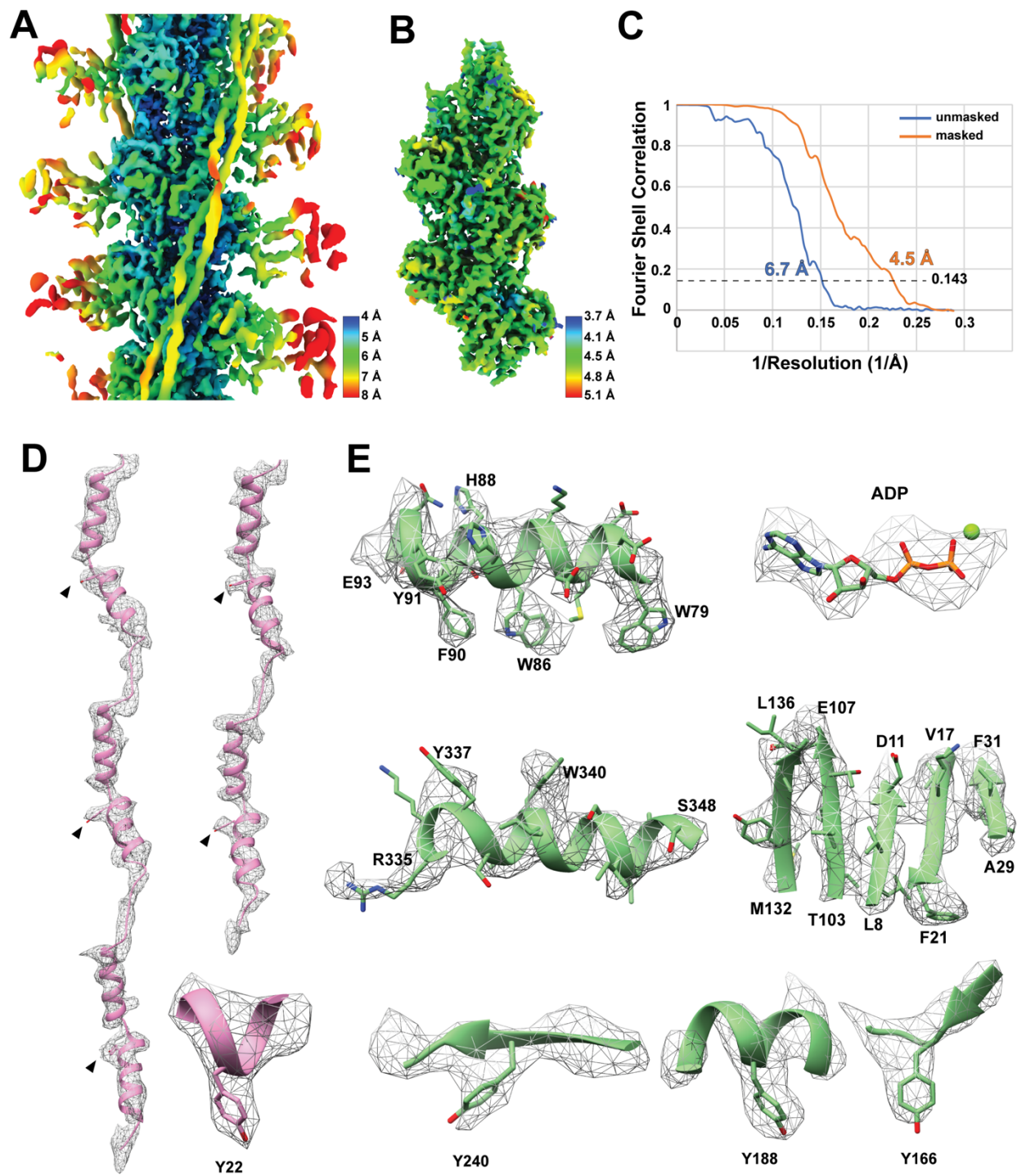


Fig. S2. EM density map and structural model of actin and nebulin obtained from sub-tomogram averaging. (A) Local resolution estimation of the unmasked thin filament. The map is filtered to local resolution. (B) Local resolution estimation of the masked core of the thin filament including actin and nebulin. (C) Gold-standard FSC curve of the actin-nebulin structure. The unmasked and masked structures correspond to the maps in (A) and (B), respectively. (D)

Nebulin model and corresponding cryo-EM density map. The conserved tyrosine residues are marked with arrow heads. A zoom-in view of an example of tyrosine 22 and corresponding density is shown. **(E)** Examples of side chain density visible in the actin portion of the cryo-EM density map. A few tyrosine residues are selected for comparison with the tyrosine side chain densities in nebulin.

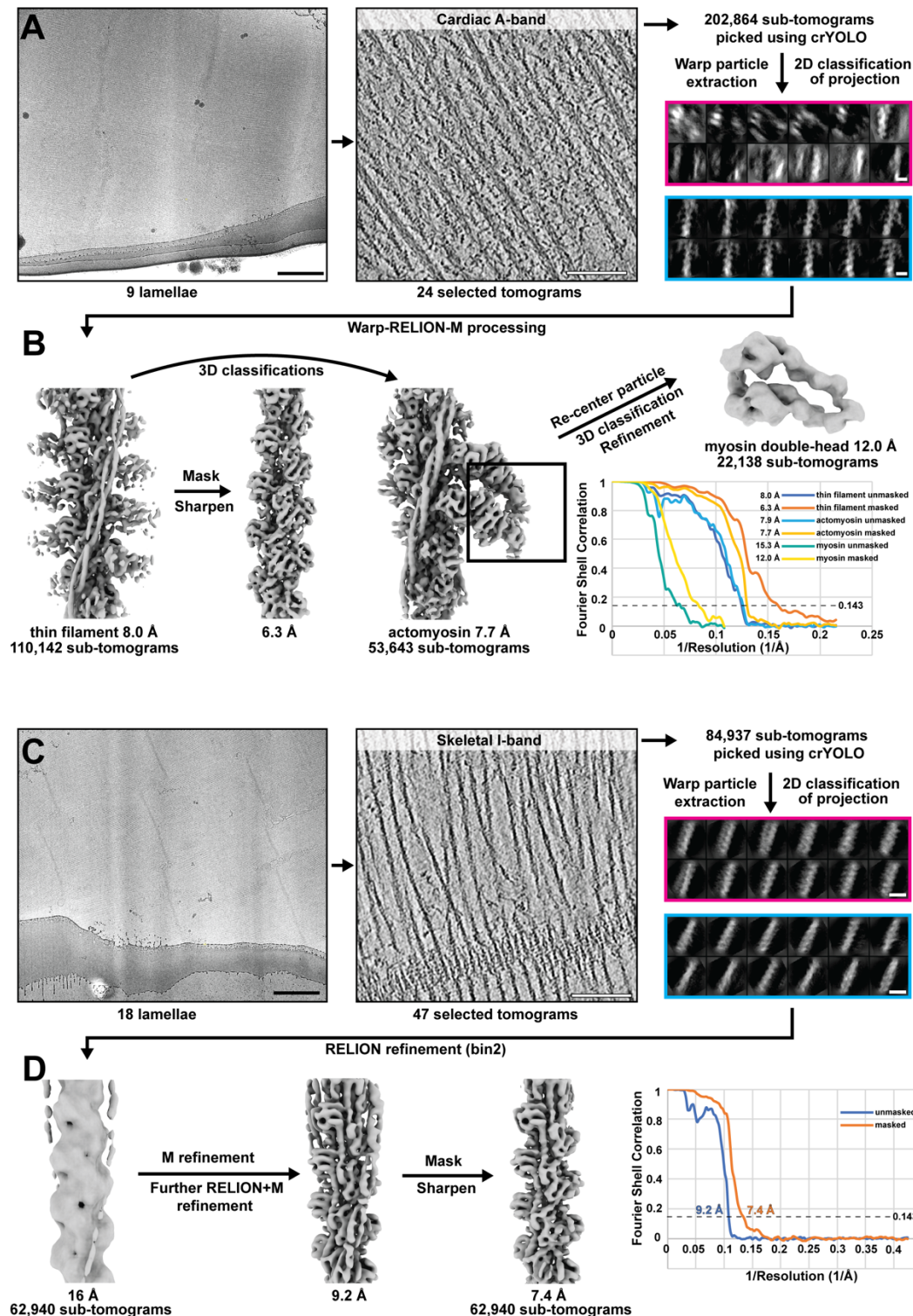


Fig. S3. Cryo-FIB-ET and processing workflow of A-band thin filament structures from mouse cardiac muscle and I-band thin filament structures from mouse psoas muscle. (A) Examples of a lamellae of mouse cardiac myofibrils, a slice through a tomogram of mouse cardiac sarcomere A-band and particle-cleaning using 2D classification. **(B)** EM density maps and gold-standard FSC curves of the thin filament, actomyosin and re-centred myosin double-head structures. The processing workflow is similar to the processing of mouse skeletal A-band

structures. **(C)** Examples of a lamellae of mouse psoas myofibrils, a slice through a tomogram of mouse skeletal sarcomere I-band (also depicting a Z-disc at the bottom) and particle-cleaning using 2D classification. **(D)** Processing workflow of the I-band thin filament and gold-standard FSC curve of the structure.

Scale bar: 1 μm (lamella), 100 nm (tomogram), 10 nm (2D classes)

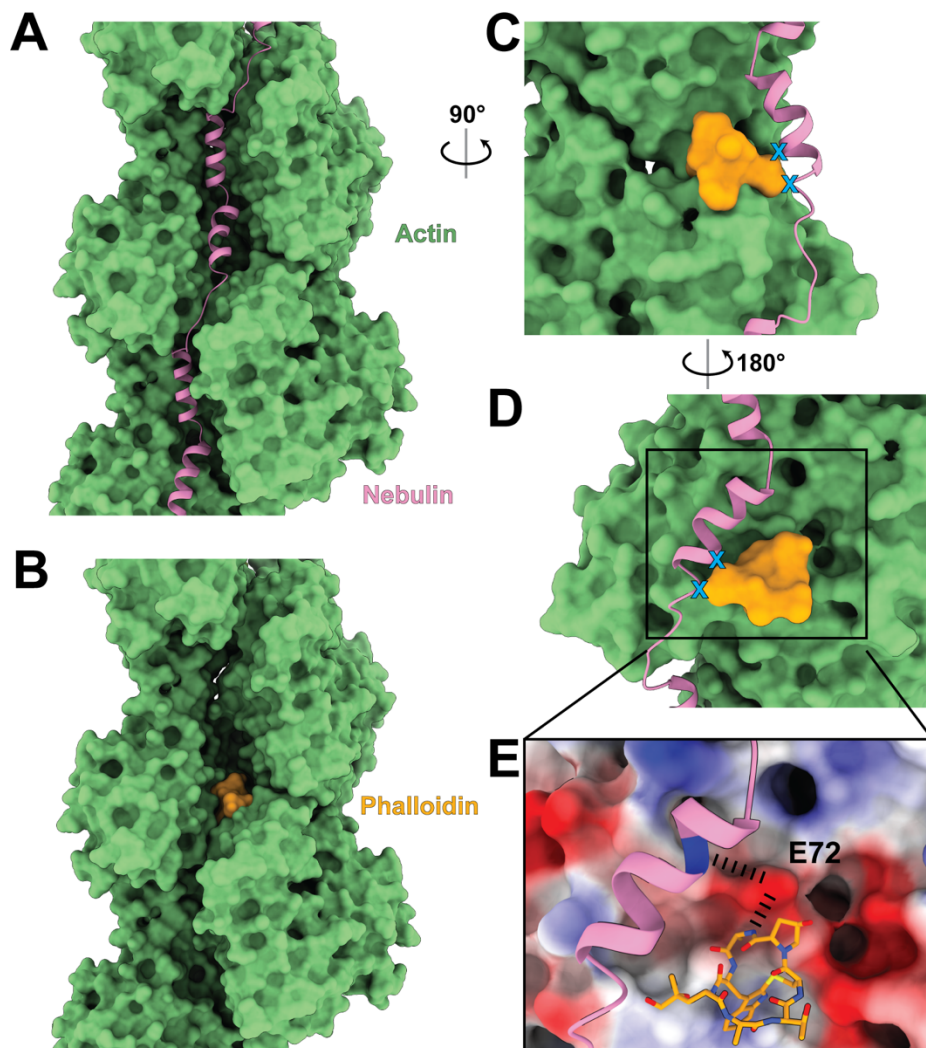


Fig. S4. Comparison of nebulin and phalloidin binding sites on the actin filament. (A,B) Position of nebulin and phalloidin (from PDB: 6T1Y) on the actin filament, respectively. (C,D) Comparison of the position of both nebulin and phalloidin from different views. Steric clashes would happen at the end of H2 of nebulin if both were present at the same time (marked by blue crosses). (E) E72 on actin is involved in both forming a hydrogen bond with phalloidin and electrostatic interactions with nebulin.

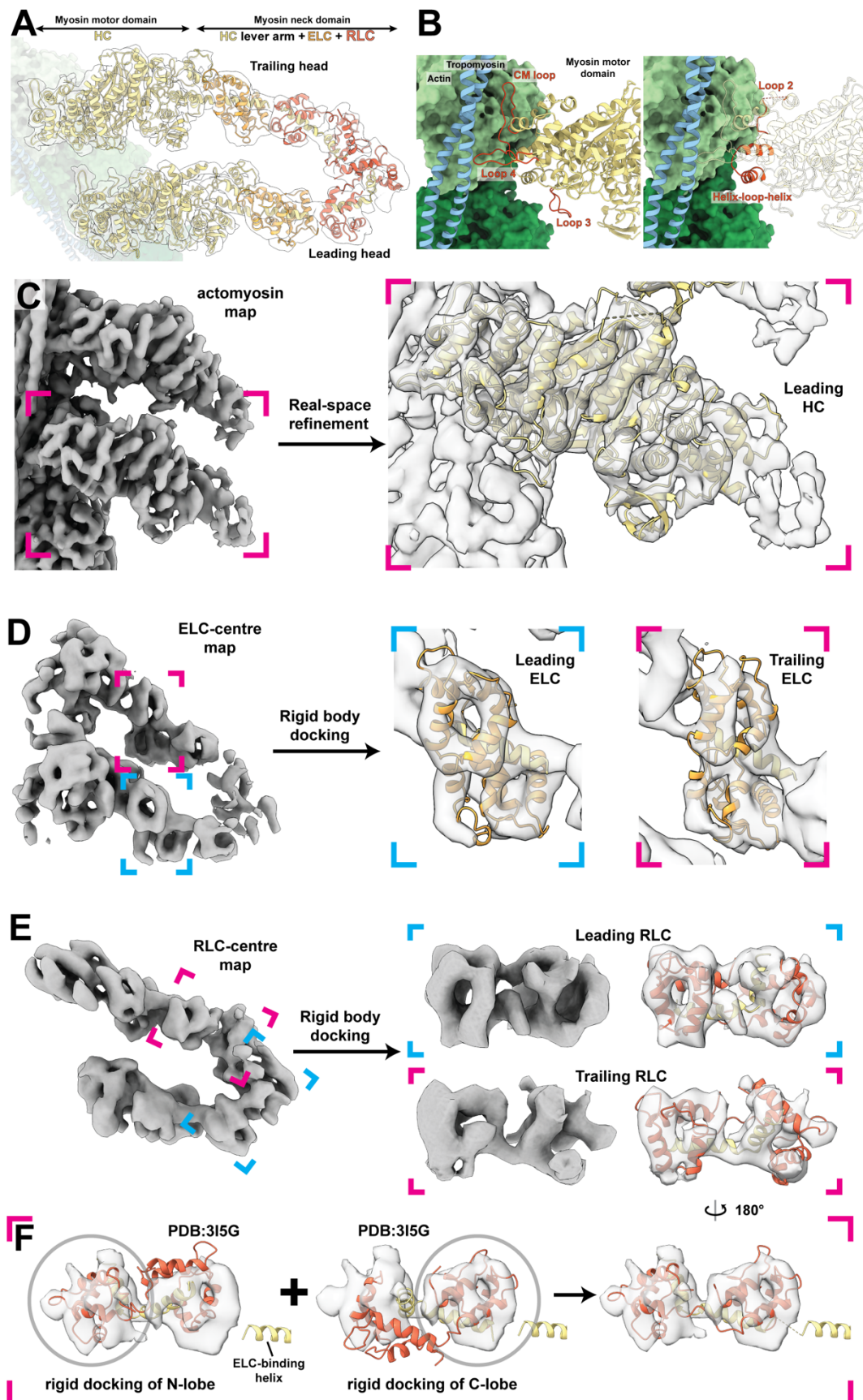


Fig. S5. Model building of myosin heads. (A) Composite EM density map and a complete structural model of a myosin double-head when bound to a thin filament. (B) Actin-myosin interaction interface. Loops on myosin involved in the interaction with actin are highlighted in red. (C) Cryo-EM density map of myosin motor domain with structural models (yellow) refined into the map. (D) Cryo-EM density map of myosin heads with a focus on the ELC. Myosin ELC (orange) and HC LH2 (yellow) from PDB 3I5G were docked into the map as rigid bodies. (E) EM density map of myosin heads with a focus on the RLC. The leading RLC density was directly fitted with the myosin RLC model (red; with HC LH3-4, yellow) from PDB 3I5G. The trailing RLC density was fitted with a modified model of RLC and HC LH3-4, as shown in (F). (F) Separate rigid body docking of the N-lobe (red; with HC LH4, yellow) and the C-lobe (red; with HC LH3, yellow) of the RLC in the trailing head. The final structural model was obtained combining the two docked models.

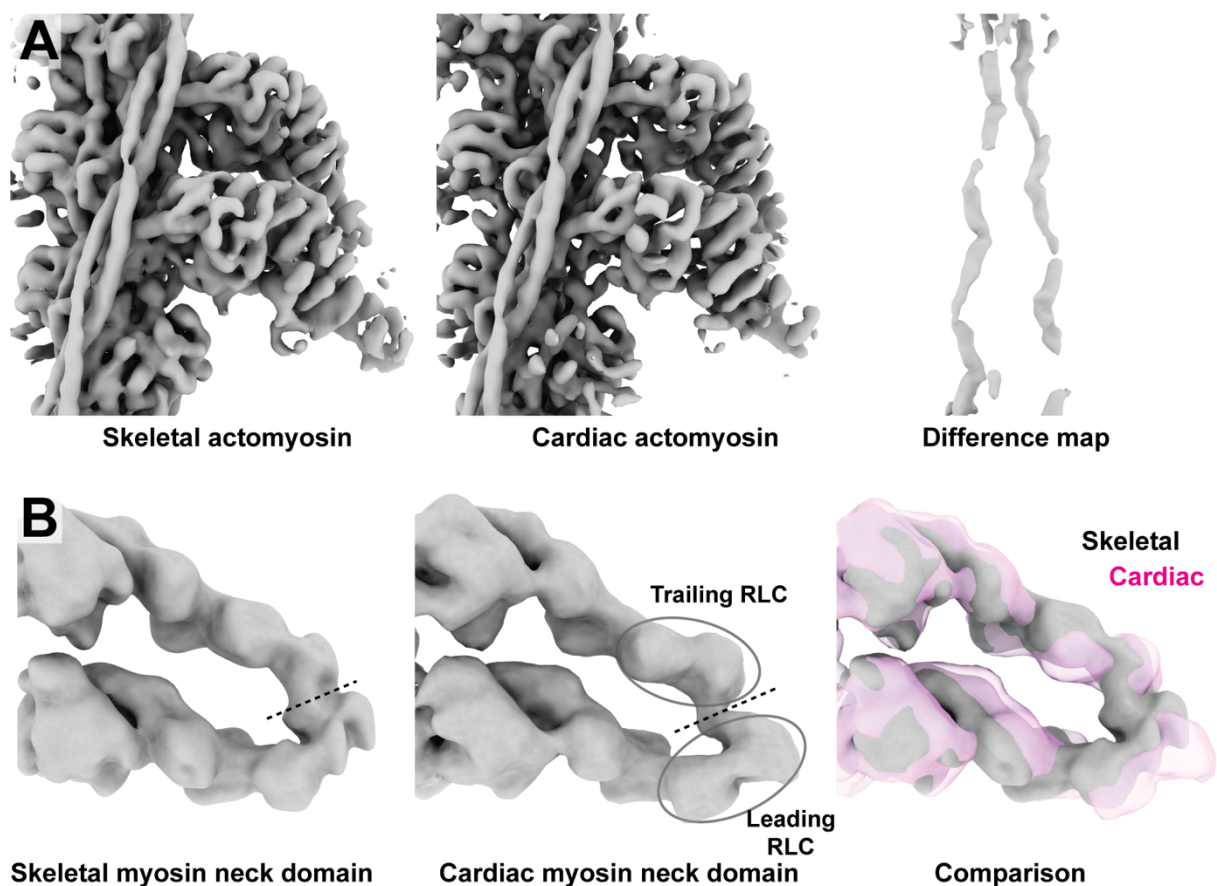


Fig. S6. Comparison between cardiac and skeletal actomyosin structures. (A) EM density maps of skeletal and cardiac actomyosin, both filtered to 7.8 Å, as well as the difference maps between them. The densities in the difference map correspond to nebulin. (B) EM density maps of skeletal and cardiac myosin double head, with a focus on the neck domain, both filtered to 15 Å. Dotted lines mark the interfaces between trailing and leading RLCs. The comparison between the skeletal and cardiac map is shown on the right.

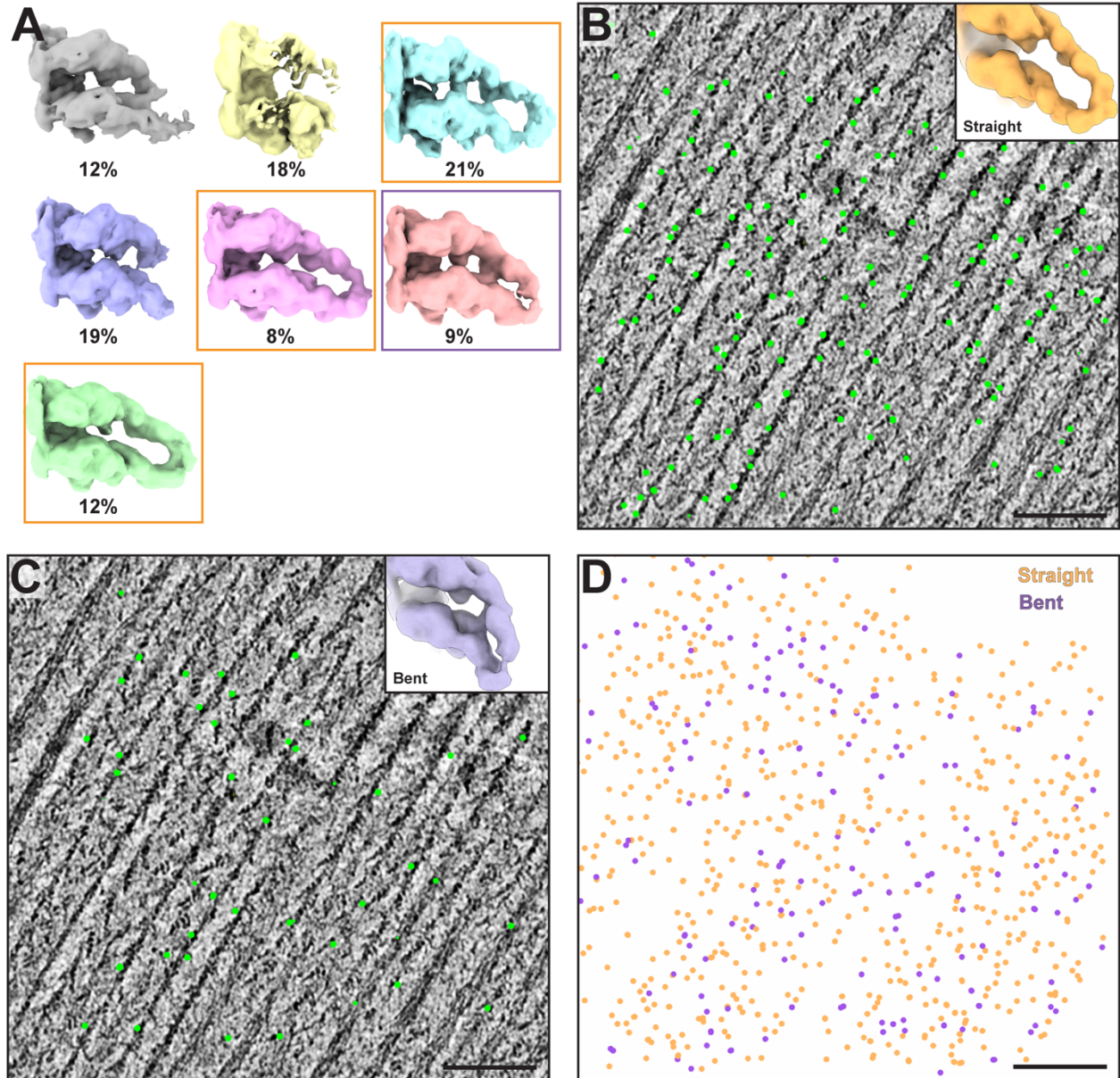


Fig. S7. Distribution of the two conformations of myosin double-head. (A) 3D classification of a myosin double-head. Classes marked in orange and purple are selected as the straight and bent form for further refinement, respectively. (B) Distribution of myosin double-head in the straight conformation in a tomogram. A slice image of the tomogram with a thickness of 14 nm and particles within it (orange) are shown. (C) Distribution of myosin double-head in the bent conformation in the same slice of tomogram as (B). Particle positions are represented in purple dots. (D) Distribution of both straight and bent forms in the entire tomographic volume. Scale bars: 100 nm.

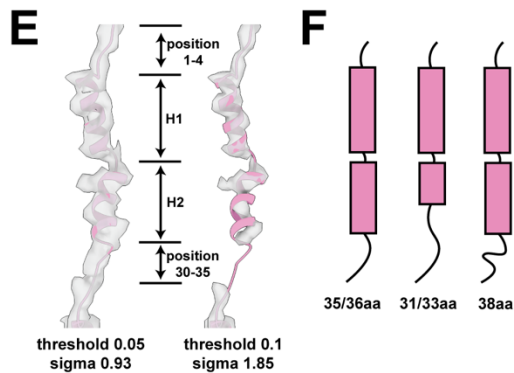
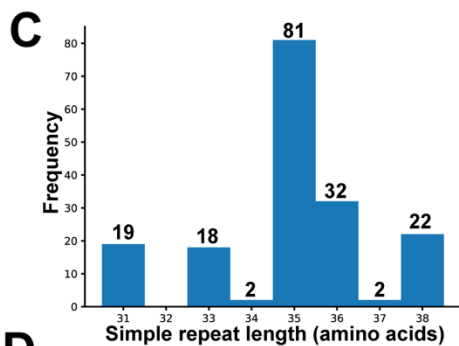
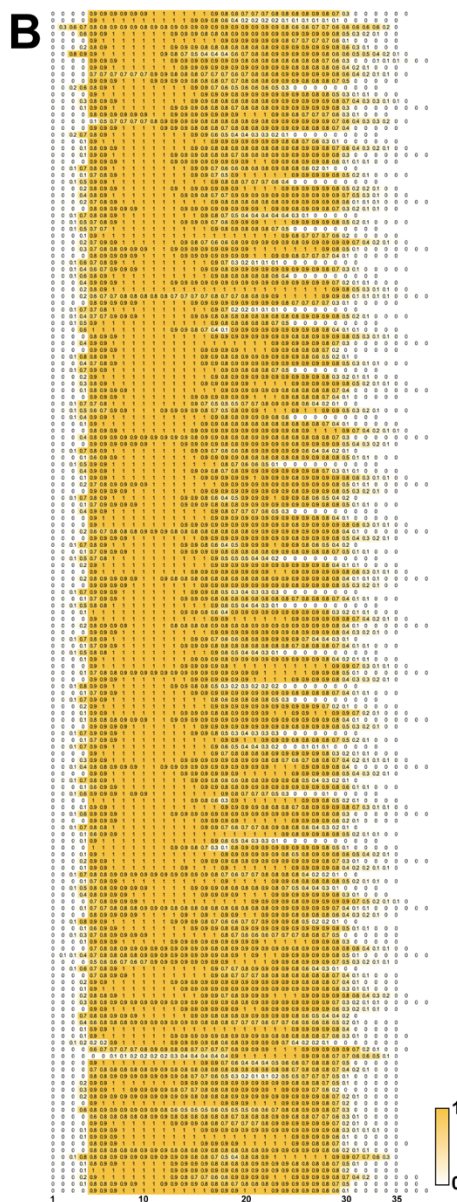
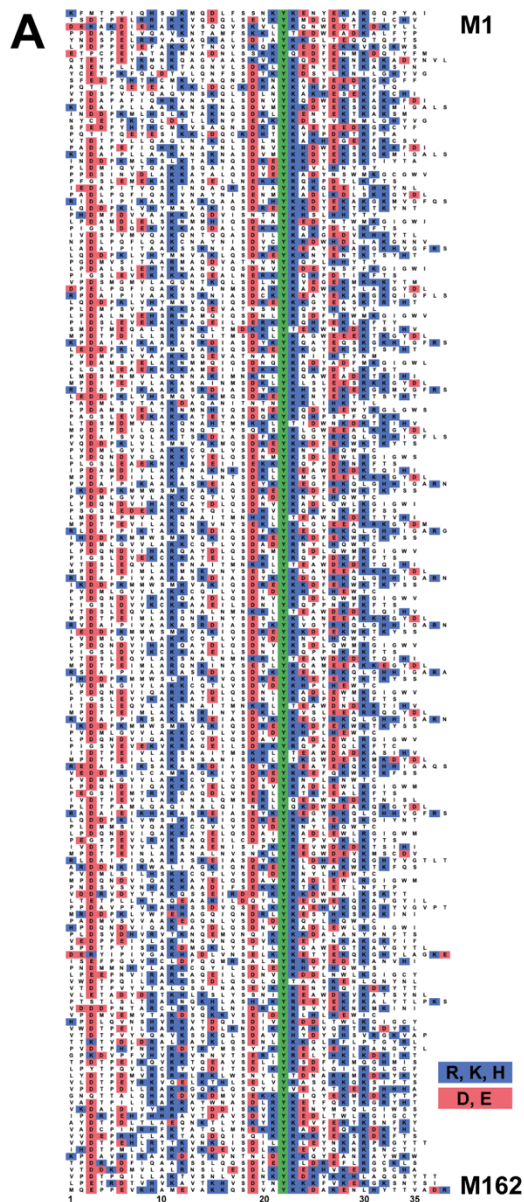


Fig. S8. Sequence, secondary structure prediction and length of individual nebulin simple repeats. (A) Sequence alignment of nebulin repeats M1-M162. Positively and negatively charged residues are highlighted in blue and red, respectively. The fully conserved tyrosine at position 22 is highlighted in green. (B) Secondary structure prediction of repeats M1-M162, coloured based on the probability of an α -helix. (C) Histogram of the length of simple repeats. (D) Averaged secondary structure prediction of normal (35/36 aa), short (31/33 aa) and long (38 aa) simple repeats. (E) Cryo-EM density map of one nebulin repeat at low and high surface threshold. (F) Schematic model of the nebulin simple repeats with different numbers of amino acids but the same physical length. α -helices are represented in magenta rectangles. Loops are shown as lines.

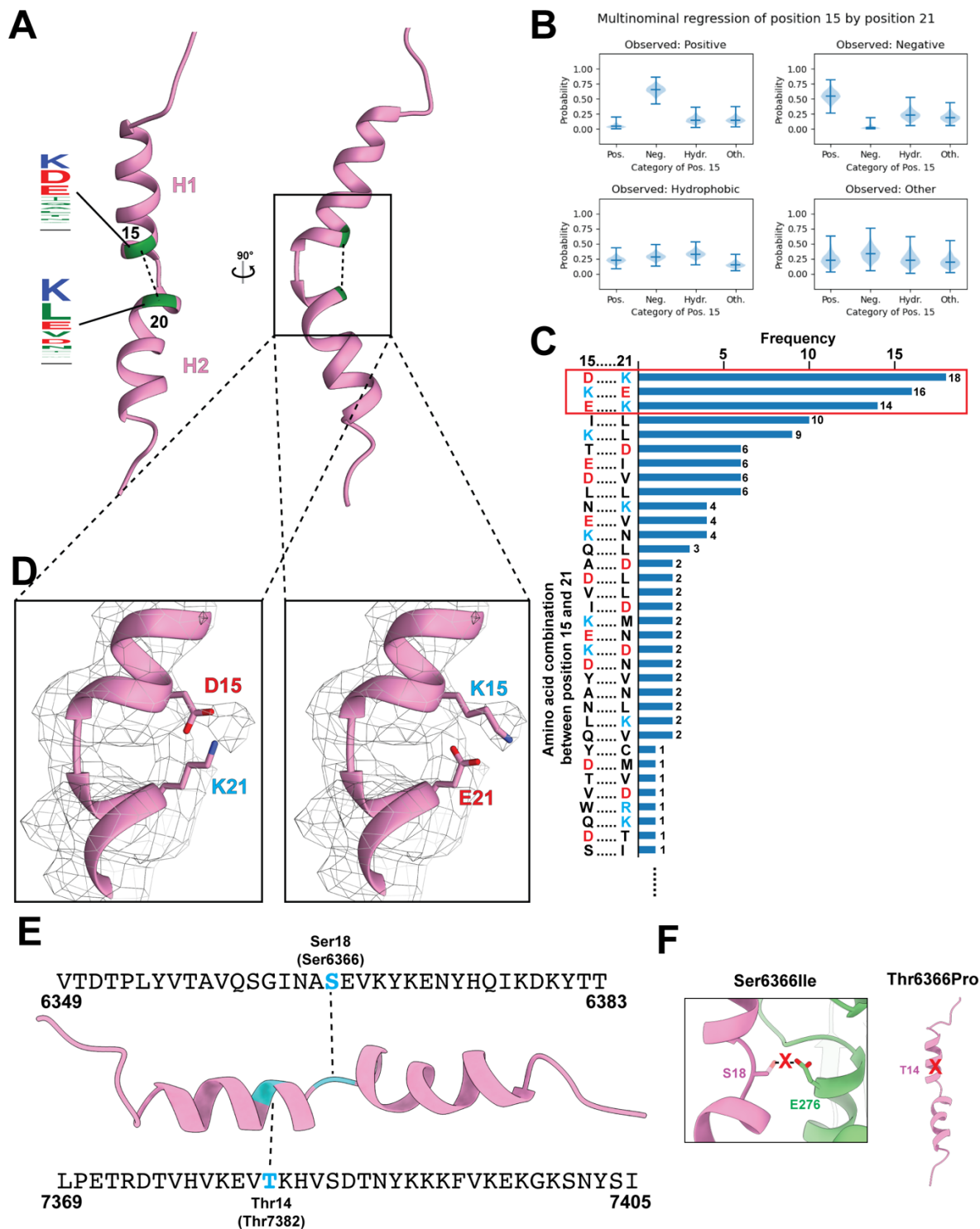


Fig. S9 Intra-nebulin interactions between position 15 and 21 and location of pathogenic missense mutations on a simple repeat. (A) Location of residue number 15 and 21 on a simple repeat including the possible amino acids at these two positions. Larger amino acid letter represents higher occurrence. **(B)** Violin plot of Bayesian multinomial regression depicting the conditional probability of a certain amino acid type on position 15 given the amino acid residue type on position 21. The median, minimum and maximum estimated probability values for each

category are shown. The shaded area shows the probability density of the model within the respective category. **(C)** Histogram of amino acid combinations of position 15 and 21. Charged amino acids are coloured in blue (positive) and red (negative). Other combinations with only one occurrence are not shown. **(D)** Weak side chain densities at position 15 and 21. Fitted structural models are mutated to the two most populated amino acid combinations at position 15 and 21 showing possible side chain conformations. **(E)** Location of the two founder mutations of nemaline myopathies in the Finnish population, S6366I and T7382P, on a simple repeat. **(F)** Potential disruption of a hydrogen bond between nebulin and E276 on actin due to the mutation S6366I and potential disruption of the H1 helix structure due to the mutation T7382P.

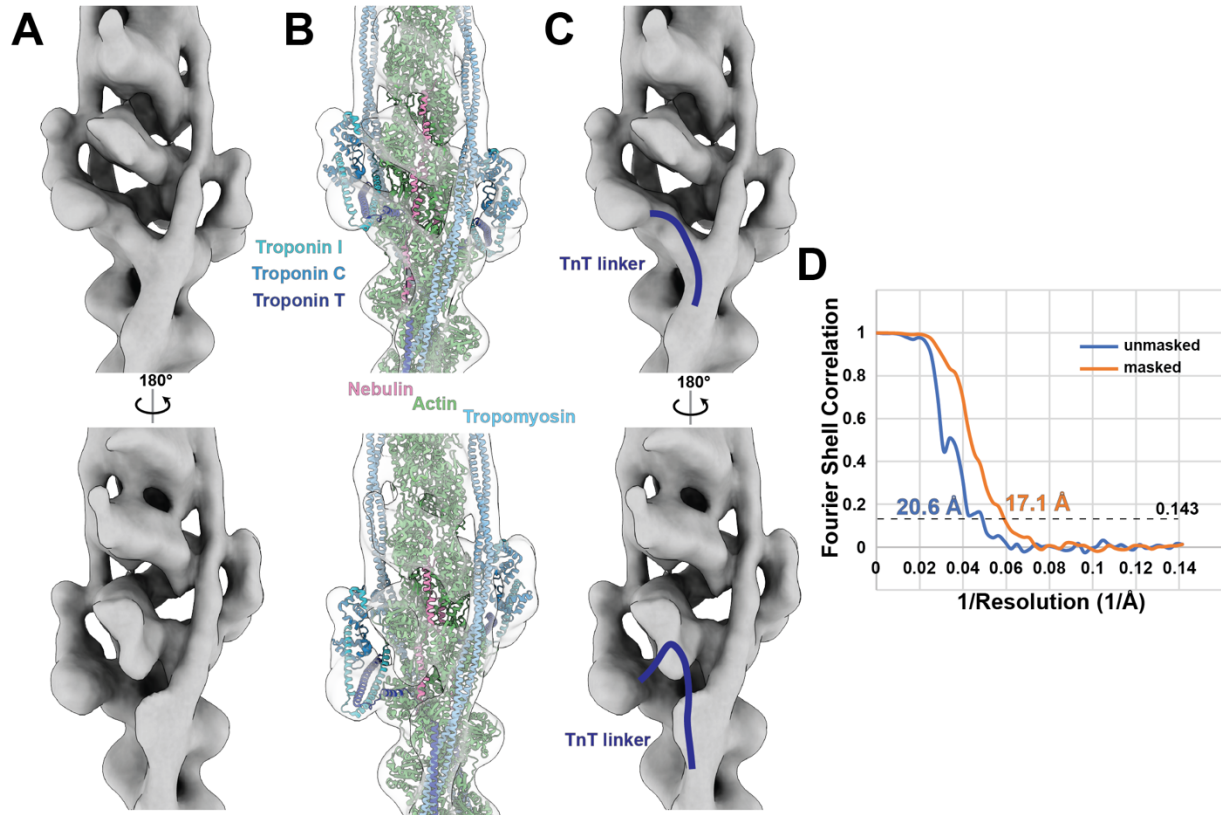


Fig. S10. Thin filament structure with troponin obtained from sub-tomogram averaging. (A) EM density map depicting the thin filament including the troponin. (B) Atomic models of actin, nebulin, tropomyosin and troponin fitted into the EM density map. (C) The position of the TnT linkers from EMD-0729 depicted on our map obtained from sub-tomogram averaging. (D) Gold-standard FSC curve of the troponin-containing thin filament structure.

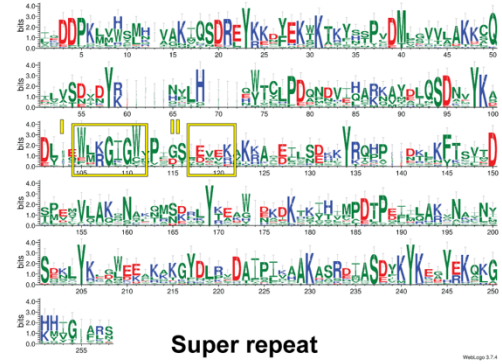
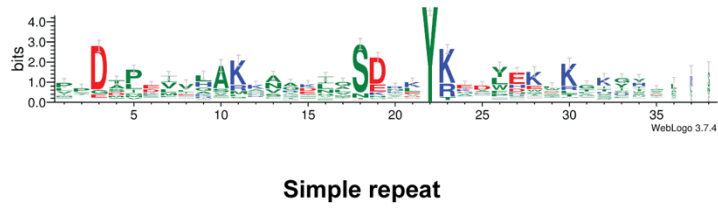
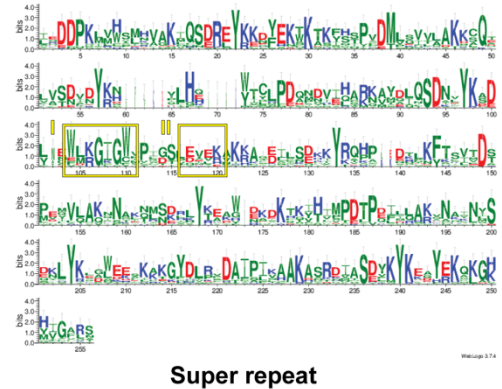
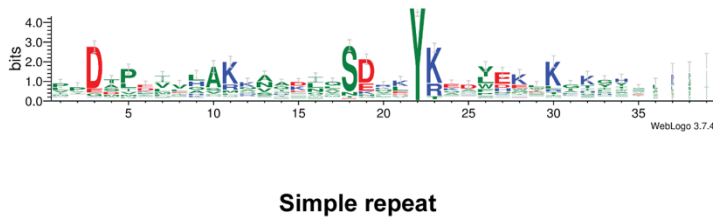
A**Mouse nebulin****B****Human nebulin**

Fig. S11. Similarities between mouse nebulin and human nebulin. (A) Sequence logos of mouse nebulin simple repeats (left) and super repeats (right) after multiple sequence alignment. (B) Sequence logos of human nebulin simple repeats (left) and super repeats (right) after multiple sequence alignment.

	Skeletal A-band				Cardiac A-band			Skeletal I-band
Microscopy								
Microscope	Titan Krios				Titan Krios			Titan Krios
Voltage (kV)	300				300			300
Camera	Gatan K2 Summit				Gatan K3			Gatan K3
Slit width (eV)	20				20			20
Pixel size (Å)	1.73				2.32			1.18
Defocus range (µm)	2.4-5.0				3.2-5.0			2.5-5.5
Tilt range ^a	-54°/+54° (3°)				-54°/+54° (3°)			-54°/+54° (3°)
Tilt scheme	Dose-symmetric				Dose-symmetric			Dose-symmetric
Total dose (e ⁻ /Å ²)	130-150				130-150			130-150
Number of lamellae	87				9			18
Number of tomograms ^b	48 (171)				24 (24)			47 (115)
3D refinement statistics	Actin-nebulin	Acto-myosin	Myosin (ELC-centred)	Myosin (RLC-centred)	Actin	Acto-myosin	Myosin (neck-domain)	Actin-nebulin
Number of sub-tomograms	141,860	104,302	44,001	44,001	110,142	53,643	22,138	62,940
Symmetry	C1	C1	C1	C1	C1	C1	C1	C1, Helical ^d (-167.4°, 28.8Å)
Resolution ^c (Å)	4.5 (6.7)	6.6 (7.2)	8.9 (10.7)	9.0 (10.1)	6.3 (8.0)	7.7 (7.9)	12.0 (15.3)	7.4 (9.2)
B-factor	-100	-75	-500	-300	-300	-200	-300	-250
EMDB deposition	EMD-13990	EMD-13991	EMD-13992	EMD-13993	EMD-13995	EMD-13996	EMD-13997	EMD-13994
Atomic model statistics								
Non-hydrogen atoms	15,550	29,589	Homology model					
Cross correlation masked	0.72	0.82						
Molprobity score	1.75	1.97						
Clashscore	17.88	30.61						
EMRinger score	0.86	0.20						
Bond RMSD (Å)	0.010	0.007						
Angle RMSD (°)	1.535	1.415						
Rotamer outliers (%)	0.00	0.00						
Ramachandran favored (%)	100.00	99.69						
Ramachandran outliers (%)	0.00	0.20						
CaBLAM outliers (%)	2.15	2.33						
PDB deposition	PDB: 7QIM	PDB: 7QIN	PDB: 7QIO					

^aTilt angle is relative to the pre-tilt of each lamella. In parenthesis is the tilt angle increment.

^bIn parenthesis is the initial number of tomograms

^cResolution is based on 0.143 FSC threshold. In parenthesis is the global resolution without mask applied.

^dHelical refinement was used for initial refinement in RELION. No helical symmetry was applied during local refinement in RELION and M.

Table S1. Data collection, refinement and model building statistics

Movie S1. Slice along Z-axis of a tomogram depicting the A-band of a mouse skeletal sarcomere.

Movie S2. Slice along Z-axis of a tomogram depicting the A-band of a mouse cardiac sarcomere.

Movie S3. Slice along Z-axis of a tomogram depicting the I-band of a mouse skeletal sarcomere.

Movie S4. Morphing between the straight and bent conformations of a myosin double-head.